JGR Solid Earth

RESEARCH ARTICLE
10.1029/2024JB028826

Key Points:

- We present an improved SNAPHU phase unwrapping method for C-band coseismic interferograms using range-offset gradients as prior information
- The proposed method enables the effective unwrapping of low-coherence regions near surface ruptures
- The method significantly improves the phase-unwrapping accuracy and aligns well with the global navigation satellite system data for three large earthquake events

Supporting Information:

Supporting Information may be found in the online version of this article.

Correspondence to:
W. Xu,
wenbin.xu@csu.edu.cn

Citation:
Jiang, K., Xu, W., & Xie, L. (2024). Unwrap intractable C-band coseismic interferograms: An improved SNAPHU method with range offset gradients as prior information. *Journal of Geophysical Research: Solid Earth*, *129*, e2024JB028826. https://doi.org/10.1029/2024JB028826

Received 30 JAN 2024
Accepted 14 SEP 2024

Author Contributions:
Conceptualization: Wenbin Xu
Data curation: Kun Jiang, Wenbin Xu
Formal analysis: Kun Jiang, Wenbin Xu, Lei Xie
Funding acquisition: Wenbin Xu
Investigation: Kun Jiang, Wenbin Xu
Methodology: Kun Jiang
Project administration: Wenbin Xu
Resources: Wenbin Xu
Software: Kun Jiang
Supervision: Wenbin Xu
Validation: Kun Jiang, Wenbin Xu, Lei Xie
Visualization: Kun Jiang
Writing – original draft: Kun Jiang
Writing – review & editing: Kun Jiang, Wenbin Xu, Lei Xie

Unwrap Intractable C-Band Coseismic Interferograms: An Improved SNAPHU Method With Range Offset Gradients as Prior Information

Kun Jiang[1], **Wenbin Xu**[1], **and Lei Xie**[1]

[1]School of Geosciences and Info-Physics, Central South University, Changsha, China

Abstract C-band Interferometric Synthetic Aperture Radar (InSAR) data are widely used to map coseismic deformation. However, phase unwrapping errors are commonly distributed near faults owing to decorrelation and steep phase gradients from short radar wavelengths. Here, we propose an improved SNAPHU phase-unwrapping algorithm that considers the prior information of the range offset gradients (P-SNAPHU) to overcome the constraints imposed by the phase continuity assumption. P-SNAPHU exploits median filtering of homogeneous pixels for initial denoising of range offset and then refines range offset gradients divisionally through saliency extraction. The derived gradients are used to estimate the expected values of the cost functions for the low-coherence fringes. The synthetic experiments show significant improvements in the phase-unwrapping accuracy of the P-SNAPHU method compared with classical unwrapping methods. We apply the P-SNAPHU method to unwrap Sentinel-1 coseismic interferograms of three large ($Mw > 6.5$) strike-slip earthquake events that the existing classical methods could not successfully unwrap. In the comparison of the unwrapped interferograms with the external global navigation satellite system (GNSS) displacements and those from the classical methods, we find that P-SNAPHU significantly reduces the phase unwrapping errors with the mean absolute error of 7.2, 2.3, and 1.8 cm for the 2023 Kahramanmaraş earthquake doublet, the 2016 Kumamoto earthquake, and the 2019 Ridgecrest earthquakes, respectively. Based on the unwrapped results derived from P-SNAPHU, an estimate is made regarding the shallow slip deficit of the 2023 Kahramanmaraş earthquake doublet, which is approximately 7%. Therefore, P-SNAPHU is useful for developing and applying C-band InSAR data for large earthquakes and volcanic activity.

Plain Language Summary Interferometric Synthetic Aperture Radar (InSAR) can obtain high-precision, wide-area ground deformation data and is essential for coseismic research of moderate to large earthquakes. However, phase unwrapping, a necessary step for InSAR to obtain accurate deformation, has historically posed a challenge for C-band data because of large deformation gradients and decorrelation near fault ruptures. Traditional unwrapping methods typically assume that surface deformation is continuous and has small gradients that fail to unwrap intense deformation regions with substantial errors when the events are large. We propose an improved phase unwrapping method based on the SNAPHU method, which leverages prior gradients from range offsets to constrain the unwrapped gradients to be solved. This method involves two crucial steps before phase unwrapping in the workflow to reduce the negative effects of the range-offset noise. We demonstrate this method using simulated data with different noise levels and real data from three large strike-slip earthquake sequences. The GNSS data from the three real cases are in good agreement with our unwrapped results and prove that the proposed method can significantly increase the phase-unwrapping accuracy near the fault rupture, which generates the largest coseismic deformation. This advancement is paramount for promoting seismic event studies using C-band SAR data.

1. Introduction

Interferometric Synthetic Aperture Radar (InSAR) is a powerful geodetic technology for studying earthquake cycle deformation owing to its wide coverage, high spatial resolution, and high accuracy in surface deformation monitoring (Bürgmann, Schmidt, et al., 2000; Elliott et al., 2016; H. Liu et al., 2023; Massonnet et al., 1993; W. B. Xu et al., 2018). Coseismic interferograms that record ground deformation from medium to large earthquakes ($Mw > 5.5$) are used to identify surface ruptures, invert fault geometry, reconstruct slip distribution, and explore dynamic mechanisms (Barnhart et al., 2016; Y. Liu et al., 2023; Wright et al., 2003; Zhao et al., 2023). However, interferograms are wrapped between $-\pi$ and π that must be unwrapped to recover the absolute deformation. This process is known as phase unwrapping. Phase unwrapping is an ill-posed problem requiring external constraints. The most realistic constraint in the spatial domain is the phase continuity assumption, which assumes the absolute difference of unwrapped phase between two neighboring pixels is less than π (Ghiglia & Pritt, 1998; Itoh, 1982). The phase continuity assumption cannot hold everywhere in interferograms due to factors such as the SAR imaging geometry, spatial sampling rate, decorrelated noise, and steep deformation gradients. The Minimum Cost Flow (MCF) method and the Statistical-Cost, Network-Flow Algorithm for Phase Unwrapping (SNAPHU) method are two classical robust methods extensively used in phase unwrapping (C. W. Chen & Zebker, 2001, 2002; Costantini, 1998). These classical unwrapping methods adopt global optimization to generate as many pixels as possible to satisfy the assumption of phase continuity, thereby suppressing the propagation of unwrapping errors (Yu et al., 2019).

The phase unwrapping of C-band coseismic interferograms of large earthquakes has been challenging because short-wavelength C-band echoes (~5.6 cm) are highly sensitive to large deformations (Bürgmann, Rosen, & Fielding, 2000; Zebker & Villasenor, 1992) making coseismic interferograms easily suffer from large deformation gradients and decorrelation near fault ruptures. The aliased fringes render it difficult to unwrap correctly, even using classical unwrapping methods, which usually underestimate the absolute value of the deformation in the near field or cause unwrapping errors to propagate to the far field. For example, the coseismic interferogram of the 2015 *Mw* 7.2 Sarez strike-slip earthquake unwrapped by the MCF produced artifacts within 10–20 km of the surface rupture (Metzger et al., 2017). The high-gradient displacement field caused by the 2016 *Mw* 7.9 Kaikōura earthquake provoked large portions of the interferograms that SNAPHU could not resolve (T. Wang et al., 2018). There are more serious unwrapping errors in the interferograms of the recent Kahramanmaraş earthquake doublet, leaving the DInSAR results of the Sentinel-1 data ineffective (Li et al., 2023; W. Wang et al., 2023).

A sidestep is to mask the near-field-wrapped phase to mitigate its adverse impact on phase unwrapping (Fielding et al., 2020; Liu et al., 2022; Yue et al., 2017), but this approach has some drawbacks. First, near-field coseismic deformation often presents complex patterns related to the kinematics of shallow crust, the mask of which hinders the characterization and analysis of shallow fault slip behavior for large strike-slip earthquakes (Milliner et al., 2015; Nissen et al., 2014; Scott et al., 2018). X. Xu et al. (2016) pointed out that the phenomenon of shallow slip deficit (SSD) may simply be a model inversion artifact in the absence of near-field geodetic data. Secondly, near-field data can capture local non-tectonic deformations, facilitating the exploration of multiple deformation mechanisms in large earthquakes (Fujiwara et al., 2017). Thirdly, masking based on coherence or manual delineation creates difficult choices. The excessive masking out of large-scale aliased fringes in coseismic interferograms of major earthquakes (e.g., 2023 Kahramanmaraş earthquakes) will ultimately lead to the overall phase unwrapping failure.

Several extensions based on traditional algorithms have been proposed to improve the unwrapping accuracy of interferograms that exhibit high-gradient characteristics caused by earthquakes, mining activities, and glaciers. Some methods attempt to minish phase gradients prior to unwrapping by multiplying the interferogram with a conjugate of rough models. The models originate from refined range offsets (Baek & Jung, 2020; Feng et al., 2023), preceding initial unwrapped results, or inverted model results from them (Dai et al., 2020; Y. Gao et al., 2023). In addition, W. B. Xu (2017) manually corrected unwrapping errors using range offsets. Vajedian et al. (2023) combined masked interferometric results and range offsets using principal component analysis to form a complete deformation map.

These preprocessing or postprocessing methods rely on the assumption of phase continuity and have certain limitations. The effectiveness of the minish strategy is highly reliant on the accuracy of the initial rough model, which should exceed 2π (Baek et al., 2018). Otherwise, the residual interferogram may fail to satisfy the phase continuity assumption leading to unwrapping errors. The theoretical precision requirement of 2π equates to approximately 2.8 cm for C-band data, a level that is challenging to attain for rough models like range offsets. Consequently, the minish strategy is not suitable for unwrapping the C-band phase. Alternative methods, such as manual correction, are time-consuming and labor-intensive, while the fusion method involving principal component analysis does not ensure the consistency of fringes.

In this study, we propose an improved SNAPHU phase unwrapping method for C-band coseismic interferograms using the gradients of range offset as prior constraints (namely, P-SNAPHU) to update the cost functions in the low-coherence region that break down the π limit. Section 2 elaborates on the principles and general workflow of the P-SNAPHU. In Section 3, we demonstrate the performance of the P-SNAPHU method for synthetic coseismic

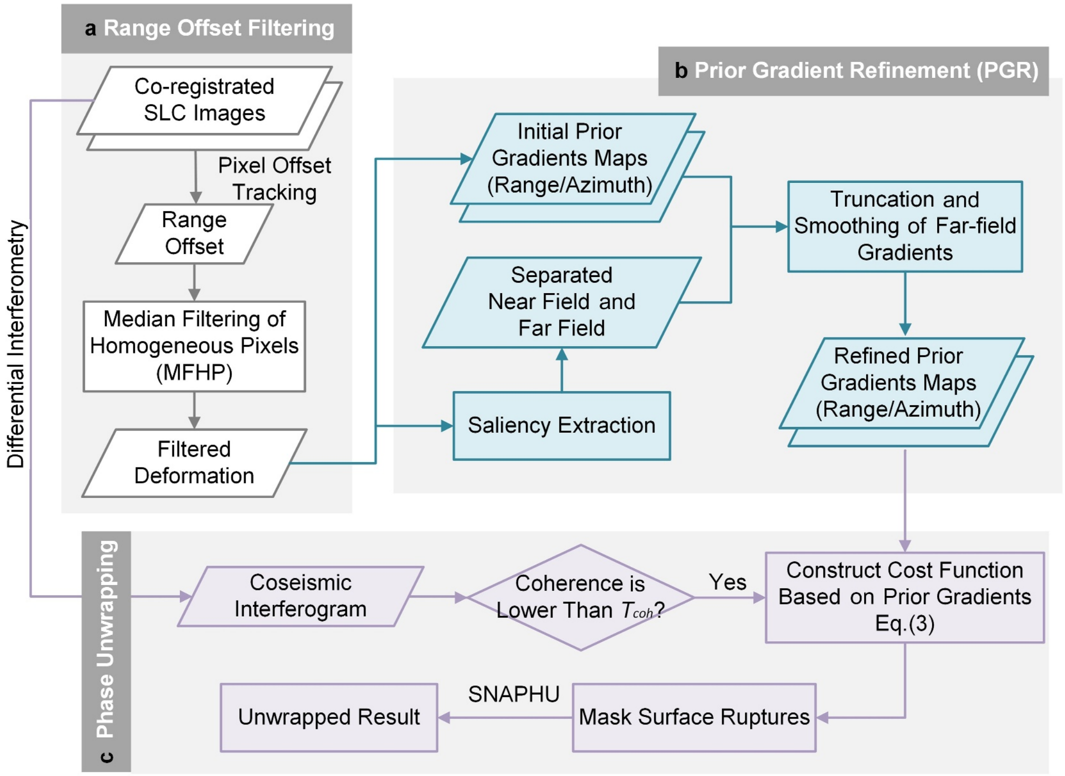

Figure 1. The schematic diagram of the proposed P-SNAPHU method.

interferograms with range offsets at different noise levels. Then, in Section 4, we apply P-SNAPHU to unwrap coseismic interferograms associated with the 2023 *Mw* 7.8 and *Mw* 7.6 Kahramanmaraş doublet, the 2016 *Mw* 7.0 Kumamoto earthquake and the 2019 *Mw* 7.1 and *Mw* 6.4 Ridgecrest earthquake sequence. The unwrapped interferograms are compared with external data (e.g., GNSS, and LiDAR). In Section 5, we discuss the effects of the coherence threshold and key preprocess steps on the accuracy of the unwrapping process using the P-SNAPHU method. Additionally, we examined the influence of various unwrapping methods on geophysical modeling, along with a discussion on the potential contributions and scalability of the P-SNAPHU method. Finally, we present our conclusions in Section 6.

2. Methodology

The P-SNAPHU method comprises three main steps: (a) medial filtering of homogeneous pixels, (b) prior gradient refinement, and (c) prior-guided unwrapping (Figure 1). To illustrate the P-SNAPHU method better, we first explain the underlying principle of the enhanced unwrapping step. Subsequently, we describe the filtering and refinement steps involved in the prior range-offset gradients measurements in the prior-based unwrapping procedure.

2.1. The Principle of P-SNAPHU

The mathematical principles utilized in the unwrapping step of P-SNAPHU are typically in alignment with those of SNAPHU. Given the input interferogram and coherence maps, phase unwrapping can be regarded as a maximum posterior (MAP) estimation problem to solve the unwrapped phase gradients. Once the unwrapped gradients are estimated correctly, the final unwrapping can be easily solved by integration. Therefore, the SNAPHU method tries to solve the set of unwrapped gradients ($\Delta\Phi$) with all known wrapped gradients ($\Delta\Psi$). The objective function in SNAPHU is a joint conditional probability density function (PDF), which is the product of the individual conditional PDFs of each gradient.

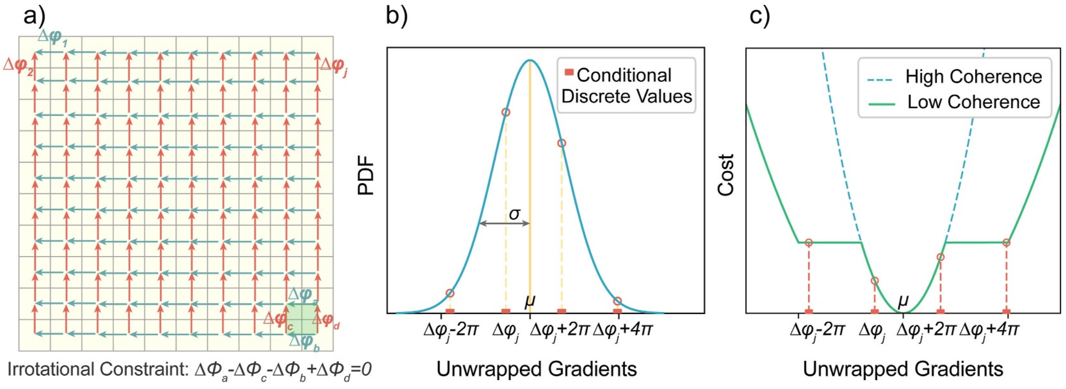

Figure 2. The principle of P-SNAPHU. (a) Wrapped phase gradients in azimuth and range directions. The light green square represents a closed loop of unwrapped phases with irrotational constraint. (b) The probability density function of the unwrapped gradient $\Delta\phi_j$ and the discrete intervals (red rectangles) conditioned by wrapped gradient $\Delta\varphi_j$. (c) Two types of cost functions with different coherence.

$$F(\Delta\Phi|\Delta\Psi) = \prod_{j=1}^{k} f(\Delta\phi_j|\Delta\varphi_j) \tag{1}$$

The $\Delta\phi_j$ and $\Delta\varphi_j$ represent unwrapped and wrapped value of gradient j, the total number of gradients in azimuth (m) and range (n) is $k = (m-1) \times n + (n-1) \times m$.

To ensure the congruence between the unwrapped and the wrapped phases, the value of $\Delta\phi_j$ should equal to $\Delta\varphi_j$ plus an integer of 2π cycles. Therefore, the conditional PDF of an unwrapped gradient is a combination of PDF $f_{\Delta\phi}(\Delta\phi_j)$ and a comb function, in which $\Delta\phi_j$ is discrete-valued (Figure 2b) as follows:

$$f(\Delta\phi_j|\Delta\varphi_j) = \begin{cases} \dfrac{f_{\Delta\phi}(\Delta\phi_j)}{\sum\limits_{a=-\infty}^{\infty} f_{\Delta\phi}(\Delta\varphi_j + 2a\pi)} & if\, \Delta\phi_j = \Delta\varphi_j + 2b\pi \\ 0 & \text{otherwise} \end{cases} \tag{2}$$

where a and b are integers. The PDF of the unwrapped gradient $f_{\Delta\phi}(\Delta\phi_j)$ is simplified as a Gaussian distribution (Figure 2b) and is determined by two factors: the mean value (μ) and the standard deviation (σ).

To simplify the nonlinear optimization process, Equation 1 is transformed into a logarithmic expression known as the cost function, and the minimization solution is:

$$\widehat{\Delta\Phi} = \text{agrmin}_{\Delta\Phi}\left\{-\sum_{j=1}^{k} \log\left[f(\Delta\phi_j|\Delta\varphi_j)\right]\right\} \tag{3}$$

In reality, the distributions of the cost function of gradients have two forms, depending on the coherence (Figure 2c). The cost of the unwrapped gradient increases as its distance from the μ value (i.e., $abs(\Delta\phi_j - \mu)$) increases. The cost distribution is similar to that of the flipped PDF. When the local coherence is poor, the cost function introduces a plateau period to allow for phase discontinuity. After the construction of all pairs of gradients, the SNAPHU method employs the dynamic-cost-cycle-canceling (DCC) algorithm for the cost-minimum solution (C. W. Chen & Zebker, 2000), which attaches an irrotational constraint to all gradients, forcing the loop closure phase to zero (Figure 2a).

Here, the P-SNAPHU method is introduced to enhance the construction of the PDF of the unwrapped gradient $f_{\Delta\phi}(\Delta\phi_j)$. The conventional SNAPHU method relies on the average wrapped gradients (G_{INF}) within a local window as an estimate of μ, and estimates σ according to the coherence. The wrapped gradients are calculated from the interferogram under the assumption of phase continuity, but they may exhibit decorrelation and bias in the vicinity of ruptured faults during significant seismic events. To improve the biased PDF, the proposed P-SNAPHU method uses the gradient of range offset to estimate the mean value (μ) in the low coherence region close to the fault. Then, the PDF can be reformulated as:

$$f_{\Delta\phi}(\Delta\phi_j) = \begin{cases} \dfrac{1}{\sqrt{2\pi\sigma}} \exp\left(-\dfrac{(x - G_{RO})^2}{2\sigma^2}\right) & \text{if coherence} < T_{\text{coh}} \\ \dfrac{1}{\sqrt{2\pi\sigma}} \exp\left(-\dfrac{(x - G_{INF})^2}{2\sigma^2}\right) & \text{otherwise} \end{cases} \tag{4}$$

where G_{RO} and G_{INF} represent the gradients from the range offset and wrapped interferogram, respectively. T_{coh} controls the level of the prior gradients from the range offset in the PDF.

The purpose of the first two steps in the P-SNAPHU method is to obtain reliable prior gradients G_{RO} through special filtering and refinement of range offset for establishing the PDF. These two steps will be explained in detail in the following Sections 2.2 and 2.3.

2.2. Median Filtering of Homogeneous Pixels (MFHP) for Range Offsets

Range offsets are the product of pixel offset tracking (POT) technology in the range direction, which is particularly effective for monitoring deformation in the near field of large earthquakes (P. He et al., 2019; H. J. Jiang et al., 2017; Lyu et al., 2022). The accuracy of the range offsets is typically between 1/10 and 1/50 of the spatial resolution in the range direction, corresponding to 5–25 cm for Sentinel-1 data. Range offsets are prone to speckle noise because of the special features of SAR amplitude maps. Therefore, reducing the noise in the range offset is important to provide reasonable prior constraints on the gradients.

The standard median filter effectively attenuates the speckle noise of range offsets, the spatial window size of which varies from 1 to 3 km according to the noise level. However, a fixed window filtering approach may not be ideal for large surface rupture events because the characteristics of the coseismic deformation on both sides of the rupture may be completely different (Hu et al., 2021). If the median filter window spans a fault rupture, the results will be biased toward zero because the coseismic deformation across the fault has opposite signs. Therefore, near- or cross-fault processes require homogeneous pixels for filtering. Here, we propose a median filtering of homogeneous pixels method (MFHP) to maintain homogeneity in near- or cross-correlated fault areas of the range offset. We first selected an appropriate spatial filtering scale w to perform standard median filtering on the range offset. We then calculated the pixel-wise standard deviation (STD) as a local indicator by sliding a fixed window of size w over the preliminary filtered result. For pixels with std higher than the threshold T_{std}, we assume a higher probability of fault-crossing heterogeneous pixels, where specialized MFHP is necessary. We maximize the intra-class variance in the estimated window (i.e., the Otsu method) to further identify the homogenous pixels. The group with the largest difference from the center point was discarded, and the remaining group was homogeneous (Figure S1 in Supporting Information S1). The improved and standard filtering methods were compared to the ascending range offset of the 2016 Kumamoto Earthquake. It can be seen that the two results differ significantly from each other near the surface rupture, with the result by MFHP closer to the true deformation pattern (Figure S2 in Supporting Information S1).

2.3. Prior Gradients Refinement (PGR)

The prior gradient maps derived from the filtered deformation after the MFHP step are still full of noise, particularly in the far field, where the gradients are usually considered smooth and small (Figure S3 in Supporting Information S1). In this section, we attempt to refine the prior gradients because incorrect prior gradients for estimating μ values can lead to noisy unwrapped results (this will be discussed in Section 5.1).

Considering that uniform processing weakens the gradients in the near field, we refine the prior gradients regionally by separating the far and near fields through the extraction of image saliency, which is an indicator for characterizing and quantifying the degree of attraction of different regions in an image to human attention (Itti et al., 1998). It can be used to distinguish the noteworthy near field from the filtered deformation map. We used a multiscale filtering method relying on dual windows (sliding window and search window) to calculate the average

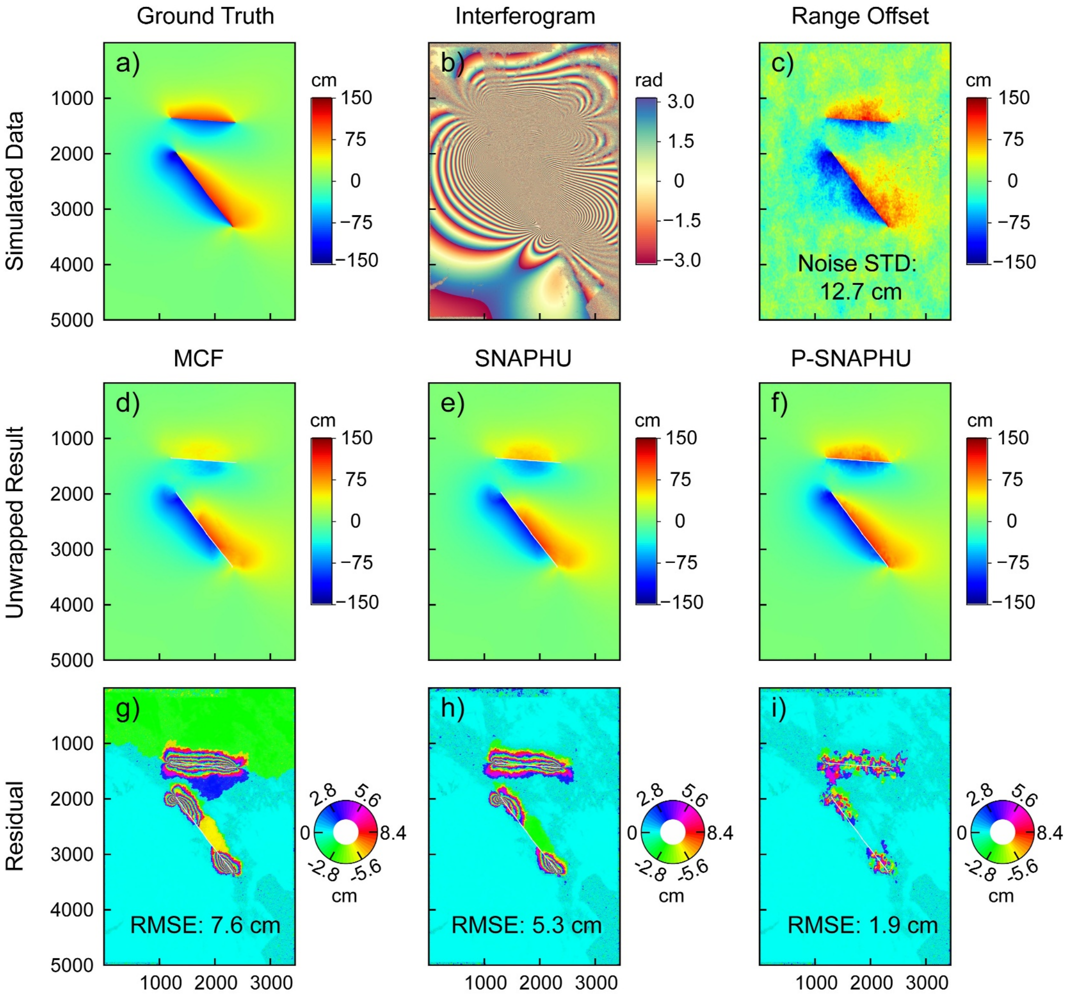

Figure 3. Simulated data and comparisons of unwrapped results by different methods. (a) The simulated original unwrapped deformation. (b) The synthetic coseismic interferogram with severe decorrelation. (c) The simulated range offset with a noise STD of 12.7 cm. (d–f) represent the unwrapped results using the classic MCF, SNAPHU, and P-SNAPHU, respectively. (g–i) represent the residual between (d–f) the unwrapped deformation and (a) the original deformation.

saliency at multiple scales (H. Gao et al., 2021). The saliency threshold, T_{sa} (approximately 0.08), was employed to delineate the far-field area, and the largest connected component was the near-field region. As the far-field gradients should follow the Itoh condition, we truncate the gradients to $(-\pi, \pi)$ in the far-field and perform large-scale mean filtering spatially.

In the P-SNAPHU method, MFHP and Prior Gradients Refinement (PGR) are two key steps that ensure the reliability of G_{RO} that affects the unwrapping accuracy directly. Following the aforementioned steps, we set up a coherence threshold T_{coh} mentioned in Section 2.1 to identify regions requiring reestimation of μ using the prior information G_{RO} (Equation 4). We found that the unwrapping effect is optimal when $T_{coh} = 0.7$ through thorough experiments (this will be discussed in Section 5.2). Moreover, it should be noted that it is better to manually mask the long and narrow surface rupture traces before unwrapping because the prior gradients across the traces are likely to be inaccurate.

3. Synthetic Experiments

To test the effectiveness of the P-SNAPHU method, we simulated a coseismic interferogram contaminated with significant decorrelation noise and compared it with other state-of-the-art unwrapping methods (Figure 3). The simulated wrapped phase contained complex Gaussian noise based on the phase gradients and coherence from a real interferogram (Figures S4a and S4b in Supporting Information S1). The noise-added, wrapped phase φ_n of the simulated interferogram can be expressed as

$$\varphi_n = \arg\left[\left(\cos\varphi_t + A_n n_R\right) + \left(\sin\varphi_t + A_n n_I\right) \times \sqrt{-1}\right] \tag{5}$$

where φ_t is the original wrapped phase, A_n takes 0–5π according to coherence and gradients, n_R and n_R represent random Gaussian noise with a mean value of zero, $\arg(\cdot)$ is the argument of the complex number. Adaptive spectral filtering was then applied to the noise-added simulated interferogram, and the coherence map was re-estimated (Figure S4c in Supporting Information S1). We simulated the input prior range offsets using Perlin noise (Perlin, 1985), in which different frequencies reproduced the spatial morphology of the speckle noise. We used normalized Perlin noise with randomly varying amplitudes to produce a series of simulated range offsets with different noise levels. The STD was between 5 and 25 cm. The simulated range offsets were spatially correlated, and the noise distribution was subjected to a Gaussian distribution (Figures S5a–S5c in Supporting Information S1). The noise-added simulated interferogram was unwrapped using the MCF, SNAPHU, and P-SNAPHU methods (Figures 3d–3f). The unwrapping residuals are discontinuous and concentrated at integer multiples of 2π (i.e., 2.8 cm for the C-band), which aligns with the fundamental principles of phase unwrapping (Figures 3g–3i). The noise observed in the residual maps that deviates from these integer multiples of 2.8 cm is attributed to decorrelation noise. Both MCF and SNAPHU produced significant unwrapping errors in the near field with RMSE of 7.6 and 5.3 cm, respectively. In contrast, the result from P-SNAPHU using the range offset with a noise STD of 12.9 cm (Figure 3c) showed only slight discrepancies in the near field (RMSE = 1.9 cm). This can be attributed to the noise originating from the range offset, which was used as prior information.

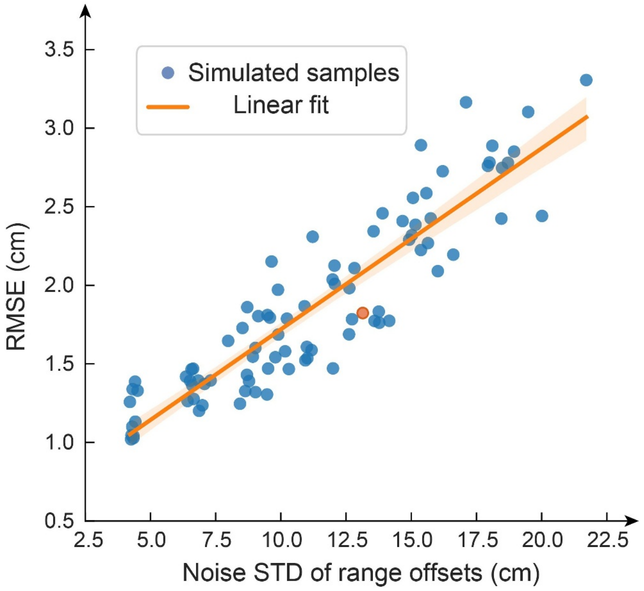

Figure 4. Relationship between the noise STD of range offsets and root mean square errors (RMSE) of unwrapped results by P-SNAPHU. The scatter points represent the unwrapped RMSE obtained using range offset samples with different noise levels. Among them, the orange scatter point is the example shown in Figure 3. The orange line indicates a good linear fit.

To further evaluate the impact of noise in prior range offsets, we applied 60 simulated samples as prior information to unwrap the interferogram using P-SNAPHU and obtained the RMSE of the unwrapped results (Figure 4). As expected, the RMSE increased as the noise STD of the range offsets increased, indicating a clear positive correlation. We found that the overall errors obtained by the P-SNAPHU method were relatively small when the noise STD of the range offsets fell within the normal range of real situations (i.e., 5–25 cm). Even when the noise STD reached 20 cm, the RMSE of the unwrapped result was below 3.5 cm, which is much smaller than that of the traditional method. More commonly, the noise STD of the real-range offsets tends to be between 10 and 15 cm. Simulation experiments indicated an average RMSE of 1.9 cm within this range, representing a 76% and 64% improvement in accuracy compared to MCF and SNAPHU, respectively.

We selected a region with dense fringes across the fault to assess the robustness of P-SNAPHU in handling coherence and phase gradient. The deformation simulation was configured with a maximum absolute value of about 1.5 m, encompassing range phase gradients ranging from −10 to 10.4 rad, and azimuth phase gradients between −20.7 and 7.5 rad (Figure S6 in Supporting Information S1). Various range offsets were employed with noise standard deviations (STDs) ranging from 1 to 26 cm to unwrap interferograms with coherence of 0.4, 0.6, 0.8, and 1.0, respectively (Figures S7a–S7d in Supporting Information S1). Comparative analysis between P-SNAPHU and SNAPHU revealed that, with the exception of scenarios with poor coherence (0.4), the root mean square error (RMSE) generally increased with larger phase gradients and was directly related to the noise level of the range offset (Figure 5). Quantitatively, the RMSEs derived from the P-SNAPHU method show that over 95% of pixels exhibit values lower than 0.1, 0.12, 0.25, and 0.55 m in interferograms with coherence levels of 1.0, 0.8, 0.6, and 0.4, respectively. Conversely, the RMSE upper limits for 95% of pixels obtained through the conventional SNAPHU method are 0.13, 0.19, 0.60, and 0.93 m, respectively. Furthermore, the P-SNAPHU method shows good performance in noise robustness. The difference between P-SNAPHU and SNAPHU is especially evident when coherence falls below 0.8 and the absolute phase gradient surpasses π, indicating that P-SNAPHU exhibits robust performance in scenarios characterized by low coherence and high phase gradient.

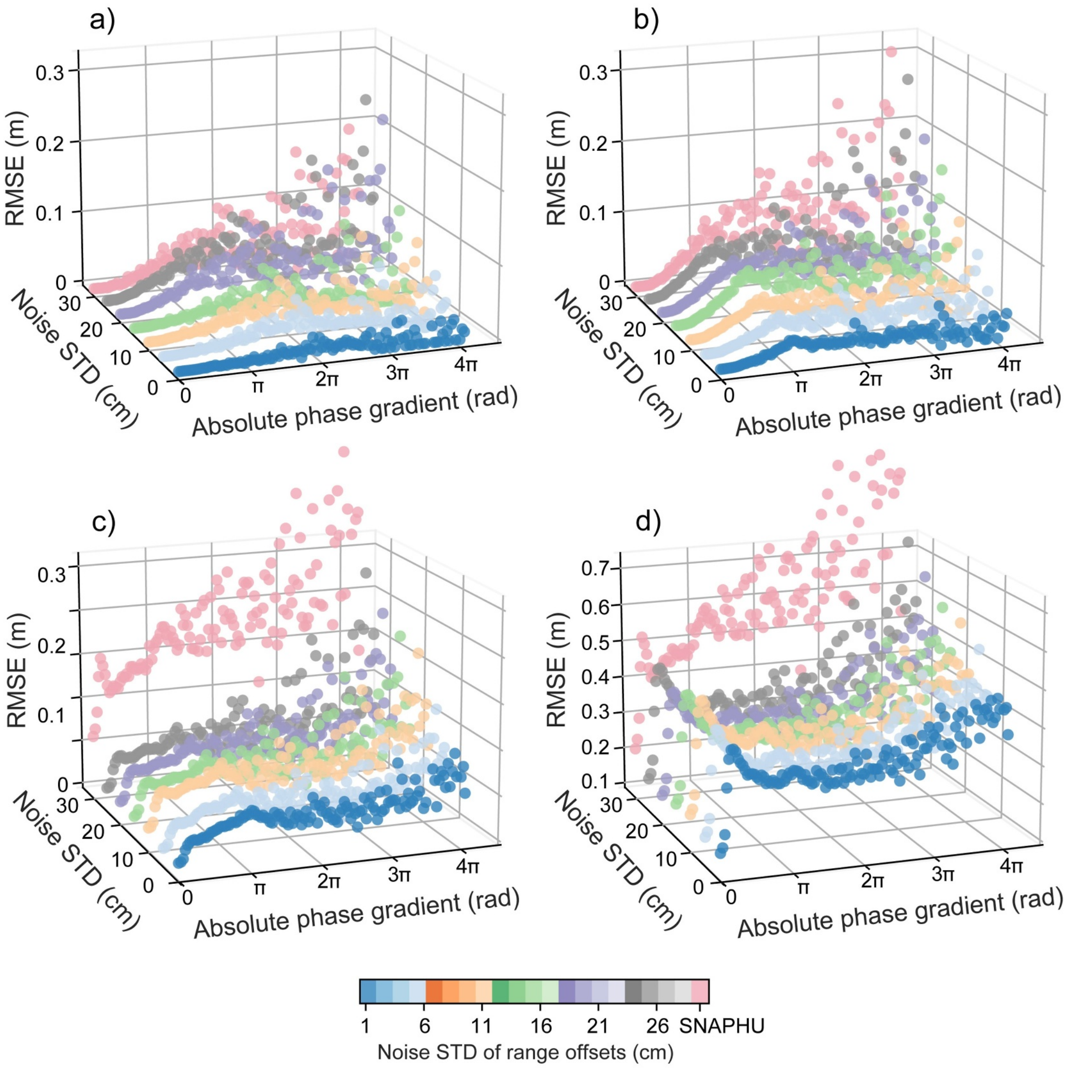

Figure 5. RMSEs of unwrapped pixels with different absolute phase gradients using the P-SNAPHU method with noise STDs of range offsets. (a–d) represent the statistical results for interferogram coherence values of 1.0, 0.8, 0.6, and 0.4, respectively. The pink scattered points represent the unwrapped results using the conventional SNAPHU method. The noise STDs are 1, 6, 11, 16, 21, 26 cm for visualization.

These findings can be utilized as a benchmark for the theoretical assessment of the accuracy of the P-SNAPHU method. In practical applications, the specific accuracy achieved is influenced by a combination of factors including the noise level of range offsets, coherence of interferograms, and phase gradient, with the former two factors exerting a more significant impact on accuracy.

4. Application on Three Major Earthquake Events

We applied the P-SNAPHU method to three large earthquake sequences with evident strike-slip surface ruptures. The three earthquake events are the 2023 *Mw* 7.8 and *Mw* 7.6 Kahramanmaraş earthquake sequence, the 2016 *Mw* 7.0 Kumamoto earthquake, and the 2019 *Mw* 7.1 and *Mw* 6.4 Ridgecrest earthquake sequence. The C-band Sentinel-1 coseismic interferograms of these events have varying degrees of difficulty in unwrapping using the traditional unwrapping method (Fielding et al., 2020; H. J. Jiang et al., 2017; Li et al., 2023). The Kahramanmaraş event is a recent hotspot and produced severe and widespread decoherent noise due to its large magnitude, whose C-band Sentinel-1 coseismic interferograms have not yet been successfully unwrapped. The Kumamoto event features more GNSS stations and LiDAR data, and can better verify the unwrapping accuracy of the P-SNPAHU method. The Ridgecrest event shows relatively higher coherence and has only a few unwrapping

Table 1
Details of the Coseismic Interferograms and Processing Parameters

Earthquake events	Track	Primary image	Secondary image	Window size w of MFHP (km)	STD threshold T_{std} of MFHP	Saliency threshold T_{sa} of PGR
2023 Kahramanmaraş	AT14	20230128	20230209	~3.5	0.3	/[a]
	DT21	20230129	20230210	~3.5	0.3	0.05
2016 Kumamoto	AT156	20160408	20160420	~2.5	0.3	0.08
	DT163	20160327	20160420	~2.5	/[a]	/[a]
2019 Ridgecrest	AT64	20190704	20190710	~1.5	0.05	0.015
	DT71	20190704	20190716	~1.5	0.05	0.015

Note. AT, Ascending Track; DT, Descending Track. [a]No threshold but process manually.

errors near the surface ruptures, offering a valuable opportunity to assess the suitability of the P-SNAPHU method in straightforward scenarios.

During processing of the Sentinel-1 SAR data, we performed an azimuth spectral deramping operation on co-registered single-look complex (SLC) images. Next, the deramped registered SLC images were used to form interferograms and range offsets. The size of the matching window for the amplitude cross-correlation calculation of the range offsets was set to 300 × 60 pixels. Flat-earth and topographic phases were removed by precision orbit and external 30 m resolution SRTM DEM. All the coseismic deformation interferograms and range offsets were multi-looked at by factors of 20 and 4 in the range and azimuth directions, respectively. Table 1 lists the details of the coseismic interferograms of these events for unwrapping and the parameters used in the application.

These interferograms were first unwrapped using the MCF and SNAPHU methods. Note that we only masked the long and narrow areas near the surface ruptures during phase unwrapping to fully compare the unwrapping effects of each method. In addition, we used a semi-variogram fitting method to quantify the noise levels of the different range offsets (Sudhaus & Sigurjón, 2009). The root of the sum of the nugget and sill variance values is thought to be the estimated noise STD of the range offsets. However, this estimation method may have biases because the second-order stationary assumption does not hold for range offsets (L. He et al., 2022), we used it solely for noise level evaluation rather than for quantitative calculations.

4.1. The 2023 Kahramanmaraş Earthquake Sequence

The North Anatolian Fault (NAF) and East Anatolian Fault (EAF) systems, located at the junction of the Arabian, Anatolian, and Eurasian Plates, are among the most important large-scale strike-slip active fault areas (Bletery et al., 2020; Hussain et al., 2018; Weiss et al., 2020). On 6 February 2023, Turkey experienced the largest earthquake doublet in recent decades, and both major earthquakes (Mw 7.8 and Mw 7.6) ruptured the left lateral strike-slip of the EAF. This event, known as the Kahramanmaraş earthquake sequence, caused tens of thousands of casualties. The extensive surface ruptures were at 310 and 150 km, leading to serious decorrelated noise in the interferograms (Figures 6a and 7a) and unprecedented difficulties in unwrapping the Sentinel-1 coseismic interferograms. Existing studies have primarily used L-band ALOS-2 interferograms or C-band Sentinel-1 POT results as alternatives (Barbot et al., 2023; Jia et al., 2023). Here, we applied the P-SNAPHU method to unwrap the Sentinel-1 descending and ascending interferograms mosaiced by two frames. Given the wide range and high noise of the range offsets, we increased the window size w in the MFHP and decreased the saliency threshold T_{sa} in the PGR (Table 1). For better unwrapping results, near-field separation of the ascending interferogram was performed by manual masking instead of saliency extraction.

We compared the range offsets and unwrapped results of the three methods (MCF, SNAPHU, and P-SNAPHU) as well as the LOS coseismic displacements of seven GNSS stations in the region (Figures 6 and 7, Table 2). The GNSS measurements were obtained from the Nevada Geodetic Laboratory (http://geodesy.unr.edu/). The MCF and SNAPHU methods showed a significant underestimation of the strike-slip movements for the descending interferogram. The extensive distribution of the incoherent region caused error propagation across the northwest side, resulting in an error of tens of centimeters in the far field. The results of P-SNAPHU were in excellent agreement with the range offset and GNSS, with an MAE of 5.2 cm between P-SNAPHU and the GNSS (Figures 6d–6f). Our method accomplished full-region effective unwrapping of the Sentinel-1 coseismic

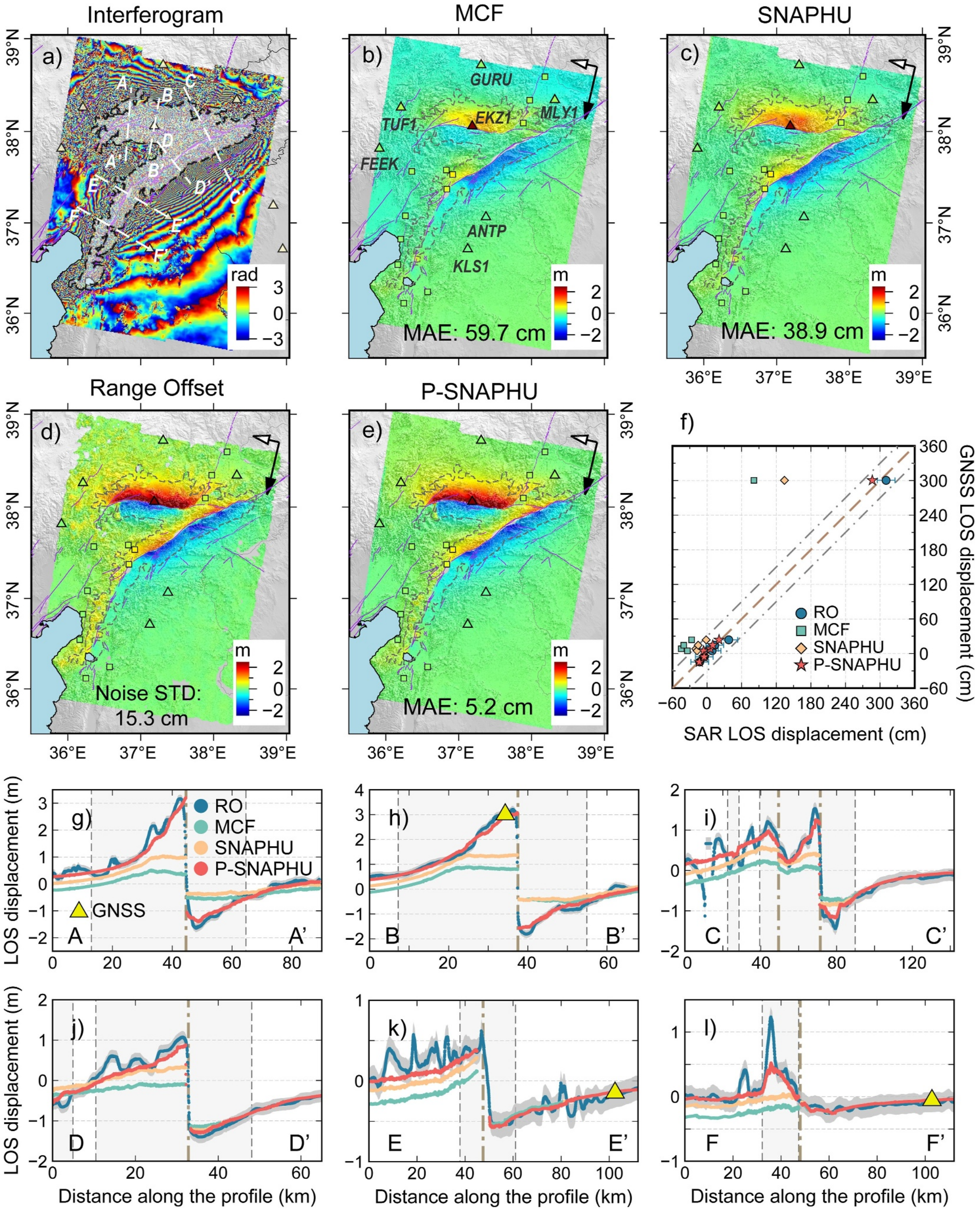

Figure 6. Unwrapped maps of the descending interferogram of the 2023 Kahramanmaraş earthquake sequence. (a) The wrapped interferogram, where yellow triangles indicate the available global navigation satellite system (GNSS) sites in this region. (b, c) The unwrapped coseismic deformation using MCF and SNAPHU, respectively. (d) The calculated coseismic range offset. (e) The unwrapped coseismic deformation using P-SNAPHU. The positive (red) and negative (blue) values indicate relative ground motion away from and toward the SAR satellite. The colored triangles in (b–e) display the GNSS displacements projected to the LOS direction. The colored squares in (b–e) display the strong-motion derived displacements projected to the LOS direction. The thin purple lines outline the active faults. The black dashed lines in (a–e) depict the separated near-field boundary by saliency extraction. (f) Comparison of projected GNSS LOS displacements from all 7 stations and the SAR LOS displacements. (g–m) Fault perpendicular profiles (AA'–FF') in (a) of LOS displacement derived from different data sources. The shading boxes denote the near-field areas, and the brown dash lines represent the locations of the surface ruptures. RO, range offset. MAE is the mean absolute error between all 7 GNSS stations and the Interferometric Synthetic Aperture Radar unwrapped result.

interferogram of this event for the first time. Significant deformation occurred close to the rupture, particularly at the EKZ1 station. The GNSS and P-SNAPHU methods calculated LOS deformations of 300.3 and 286.5 cm, respectively. The difference between these two measurements is just 13.8 cm, whereas other unwrapping

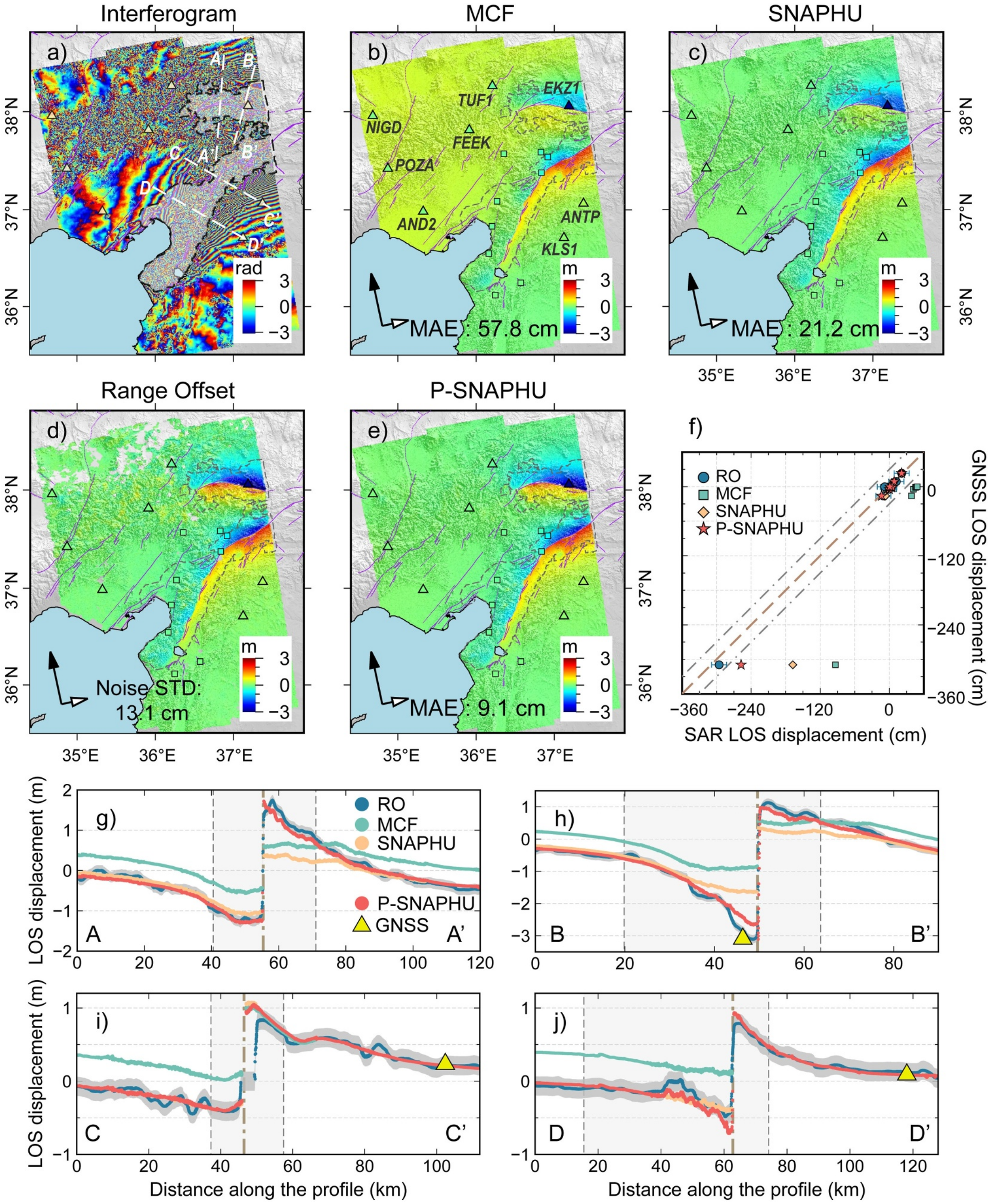

Figure 7. Unwrapped maps of the ascending interferogram of the 2023 Kahramanmaraş earthquake sequence. (a) The wrapped interferogram, where yellow triangles indicate the available global navigation satellite system (GNSS) sites in this region. (b, c) The unwrapped coseismic deformation using MCF and SNAPHU, respectively. (d) The calculated coseismic range offset. (e) The unwrapped coseismic deformation using P-SNAPHU. The positive (red) and negative (blue) values indicate relative ground motion away from and toward the SAR satellite, respectively. The colored triangles in (b–e) display the GNSS displacements projected to the LOS direction. The colored squares in (b–e) display the strong-motion derived displacements projected to the LOS direction. The thin purple lines outline the active faults. The black dashed lines in (a–e) depict the separated boundary of the near-field by manually masking. (f) Comparison of projected GNSS LOS displacements from all 8 stations and the SAR LOS displacements. (g–j) Fault perpendicular profiles (AA'–DD') in (a) of LOS displacement derived from different data sources. The shading boxes denote the near-field areas, and the brown dash lines represent the locations of the surface ruptures. RO, range offset. MAE is the mean absolute error between all 8 GNSS stations and the Interferometric Synthetic Aperture Radar unwrapped result.

techniques show differences of several hundred centimeters (Table 2). The six profiles perpendicular to the surface ruptures further demonstrate the advantages of our approach (Figures 6g–6l). The AA' and BB' profiles show that the unwrapped results closely match the range offset under strong constraints from the near-field prior gradients. It is also worth noting that the traditional methods show noticeable inconsistencies in range offset in the

Table 2
Comparison of Coseismic LOS Deformations Obtained by Different Methods and GNSS Sites for the 2023 Kahramanmaraş Earthquake Doublet

GNSS station	GNSS	Range offset	MCF	SNAPHU	P-SNAPHU
Descending LOS deformation (cm)					
GURU	8.2	4.1	−44.7	−19.5	5.7
TUF1	23.8	37.6	−26.7	−1.5	20.9
EKZ1	300.3	310.5	81.3	134.3	286.5
FEEK	4.7	8.7	−34.1	−17.3	−6.1
ANTP	−14.6	−12.6	−13.4	−13.4	−13.4
KLS1	−5.7	−4.7	−5.2	−5.2	−5.2
MLY1	14.5	13.4	−40.5	−15.3	9.9
Ascending LOS deformation (cm)					
TUF1	−16.0	−10.3	38.4	−6.4	−13.5
EKZ1	−309.3	−295.6	−93.5	−167.6	−257.5
FEEK	−4.5	−0.7	41.9	−0.1	−0.1
ANTP	23.3	21.5	21.2	21.2	21.2
KLS1	8.9	12.1	8.4	8.4	8.4
ADN2	−1.2	−0.4	45.6	3.6	3.6
POZA	−0.9	−2.4	46.9	4.9	4.9
NIGD	−0.2	−8.0	48.6	1.0	1.0

distant field, which is not evident in the findings of P-SNAPHU. Profiles CC' and EE' display noticeable speckle noise in the range offset, whereas the P-SNAPHU results remain unaffected by these noises, maintaining a relatively smooth and consistent representation of the actual deformation characteristics (this is discussed in detail in Section 5). Similar noise resistibility can also be seen in profile FF', where the peak in the range offset does not indicate deformation but prominent noise.

For the ascending interferogram, the unwrapping results obtained by MCF also had serious error propagation in the far field on the northwest side, but this did not occur in the results of SNAPHU (Figures 7b and 7c). The unwrapping errors of SNAPHU were concentrated in the near field on the northeast side (Figure 7c). The results of P-SNAPHU aligned well with the range offset and GNSS, with an MAE of 9.1 cm between P-SNAPHU and GNSS (Figures 7d–7f). At the EKZ1 site, the difference between GNSS and P-SNAPHU rises to 50 cm, which is much less than the almost 100 cm difference seen with traditional methods (Table 2). This discrepancy could be attributed to the large regional decorrelated noise in the interferogram and the inclusion of the early post-seismic deformation in SAR-based results. Four profiles perpendicular to the surface ruptures further illustrate a detailed comparison between various data sources (Figures 7g–7j). Profiles AA' and BB' span the rupture trace of the *Mw* 7.6 earthquake, and the entire area along the lines is covered by severe decorrelation. In this scenario, along these profiles, the phase-unwrapping accuracy of P-SNAPHU far surpassed that of the traditional methods. Profiles CC' and DD' span the rupture trace of the *Mw* 7.8 earthquake, where decorrelation is distributed narrowly along the rupture trace; thus, except that MCF has a large error in the far field, the unwrapping results of each method for these two profiles are relatively close. Undoubtedly, the unwrapped results obtained using P-SNAPHU near the rupture were more reliable. Furthermore, the profiles CC' and DD' demonstrate the ability of P-SNAPHU to withstand range offset noise (Figures 7i and 7j).

We used the near-field strong-motion coseismic deformation data processed by C. Liu et al. (2023) to enhance the assessment of near-field unwrapping accuracy. Due to potential orientation errors affecting some strong-motion stations (C. Liu et al., 2023), we carefully selected and excluded stations with deviations larger than 25 cm from range offsets. This process left us with 12 stations for comparing the unwrapping accuracy of different methods, as detailed in Table S1 of Supporting Information S1. Overall, the MAEs of P-SNAPHU, range offset, SNAPHU, and MCF with strong-motion LOS displacements on descending orbit are 7.6, 7.9, 17.7, and 32.9 cm, respectively. The corresponding MAEs on ascending orbit are 6.8, 7.4, 6.8, and 27.0 cm, respectively. At station 4624, the recorded deformations in the LOS direction are 68.6 cm (descending) and −77.7 cm (ascending). The P-SNAPHU unwrapping results show 53.8 and −85.0 cm, respectively, indicating accuracy within the anticipated range.

4.2. The 2016 Kumamoto Earthquake

Kyushu Island, situated in southern Japan near the Nankai Trench, is intersected by the Median Tectonic Line, a fault system that accommodates oblique convergence of the Philippine Plate to the Eurasian Plate at a shear rate of 5–10 mm/year. On 16 April 2016, a large mainshock with a magnitude of *Mw* 7.0 struck central Kyushu Island and ruptured near the Futagawa Fault. Preceding the mainshock, two *Mw* > 6.0 foreshocks occurred on the adjacent Hinagu Fault. The focal mechanism indicates that the main shock is a right-lateral strike-slip with a small component of normal slip. Field investigations have revealed nearly 34 km of surface ruptures, primarily oriented NE-SW along the Futagawa Fault, reaching the western rim of the caldera of the Aso Volcano to the east and the northernmost part of the Hinagu Fault to the west (Moore et al., 2017; Shirahama et al., 2016; Yue et al., 2017). There are 23 GNSS stations from the Global Position System Earth Observation Network System (GEONET) provided by Y. Zhang et al. (2018) and Fukahata and Hashimoto (2016) and a near-field LiDAR measurement conducted by P. He et al. (2019). We used the P-SNAPHU method to unwrap both the ascending and descending interferograms spanning this event, with the results shown separately as follows:

The near-field fringes of the ascending-wrapped interferogram appeared unclear, particularly on the northern side of the Futagawa Fault (Figure 8a). We simply followed the P-SNAPHU processing flow using the range offset with an STD of 13.2 cm and a maximum surface deformation of 2 m. For comparison, we projected external 3D displacement data in the LOS direction. The LiDAR, range offset, and P-SANPHU results were consistent in terms of spatial pattern and magnitude (Figures 8d and 8e). The deformation observed at all 23 GNSS stations within the study area aligns well with the unwrapped result, exhibiting a minimal MAE of 2.3 cm (Figure 8f), compared to an MAE of 8.9 cm between GNSS and the range offset. This indicates that despite using range offsets as prior constraints, the overall accuracy of our unwrapped result is much better than that of the range offset. This enhancement can be attributed to high-precision observation in coherent regions from InSAR and the favorable recovery of deformation signals beneath the noise in decorrelated regions with the assistance of the range offset. We used three near-field GNSS stations with substantial displacement to compare P-SNAPHU and other phase-unwrapping methods (Table 3). The near-field MAE (N-MAE) for the three GNSS displacements using the proposed method is 4.6 cm, which is a significant improvement over MCF (23.8 cm) and SNAPHU (16.8 cm).

We selected four profiles intersecting the faults and unified different deformation maps in the same LOS direction: range offset, MCF, SNAPHU, P-SNAPHU, GNSS, and LiDAR. The results of our proposed method are much closer to the LiDAR, GNSS, and range offset in the near field than those of MCF and SNAPHU. For profile AA', the amplitude of the P-SNAPHU result was lower than the range offset, owing to defective near-field separation. Because the gradients were used to construct the cost functions in the near field without further processing after the MFHP, the near field was a strongly constrained area of prior information (shaded areas in the profile subfigures). In contrast, the gradient information in the far field, which is considered a weakly constrained area, is truncated and smoothed. Notably, we observed obvious decoherence in the separated far field on the side of point A (Figure 8a), where unwrapping was unexpectedly guided by the weak constraints of the range offset. Consequently, the unwrapped result did not exhibit a steep rise but increased slowly. This limitation of P-SNAPHU, caused by defective near-field separation, calls for a more intelligent approach to identify the decorrelated near field during the PGR step. In other profiles, the differences between the range offset and the P-SNAPHU result were relatively small, mainly owing to decorrelated noise and the accuracy of the range offset. When compared with LiDAR, our result showed more obvious differences than the case compared with range offset. We believe that two factors are responsible for this occurrence. The first is the error of LiDAR data. Figure S8 in Supporting Information S1 provides a detailed comparison between the LiDAR and range offset, indicating that the LiDAR data may also contain some errors owing to the acquisition method, as is evident from the prominent striped pattern in the LiDAR deformation field. The second factor comes from the limitation of P-SNAPHU itself. We found that the unwrapped result of the P-SNAPHU does not significantly surpass the range offset within the gradient constraints based on the range offset in the decorrelated near field. This limitation could be due to the inappropriate filtering of the interferogram, which results in unsuppressed decorrelated noise. However, this particular problem was not the focus of our study.

In contrast to the significant deformation feature in the ascending imaging geometry, the descending data were much more difficult to unwrap using P-SNAPHU. The growth of vegetation in the southern mountainous area and the descending image geometry decreased the SNR of the measurements (Bamler & Eineder, 2005), causing widely distributed speckle noise in the range offset (Figure 9d). Even with a stronger filter, the eastern side of the fault still contained two notable errors (Figure S9 in Supporting Information S1). As it is challenging to trade off between preserving deformation and removing noise, we tried to broaden the scope of the P-SNAPHU application by combining the LiDAR within the blue loop curve on the left (Figure 9a) with the remaining area of range offset as prior constraints. In the P-SNAPHU workflow, substantial noise blocks render the saliency analysis ineffective when isolating the near field. Manual masking was performed to complete this step. The resulting unwrapped deformation is shown in Figure 9e.

The MAE between all 23 GNSS stations and the P-SNAPHU unwrapped result is 2.3 cm (Figure 9f), presenting an extraordinary reduction compared with the MAE of 11.2 cm between GNSS and the range offset. In order to assess the accuracy of various unwrapping methods, we utilized data from four GNSS stations with significant absolute deformation values as near field data (Table 3). The N-MAE for the displacements of the four GNSS stations and our proposed method is 2.0 cm, which is less than the 4.8 cm observed in both MCF and SNAPHU methods. Four profiles perpendicular to the faults with LOS deformations from various data sources and methods are plotted in Figures 9g–9j. In profile AA', the P-SANPHU result was the closest to the GNSS deformation near the surface ruptures, confirming that the accuracy of our new result was higher than that of the range offset and

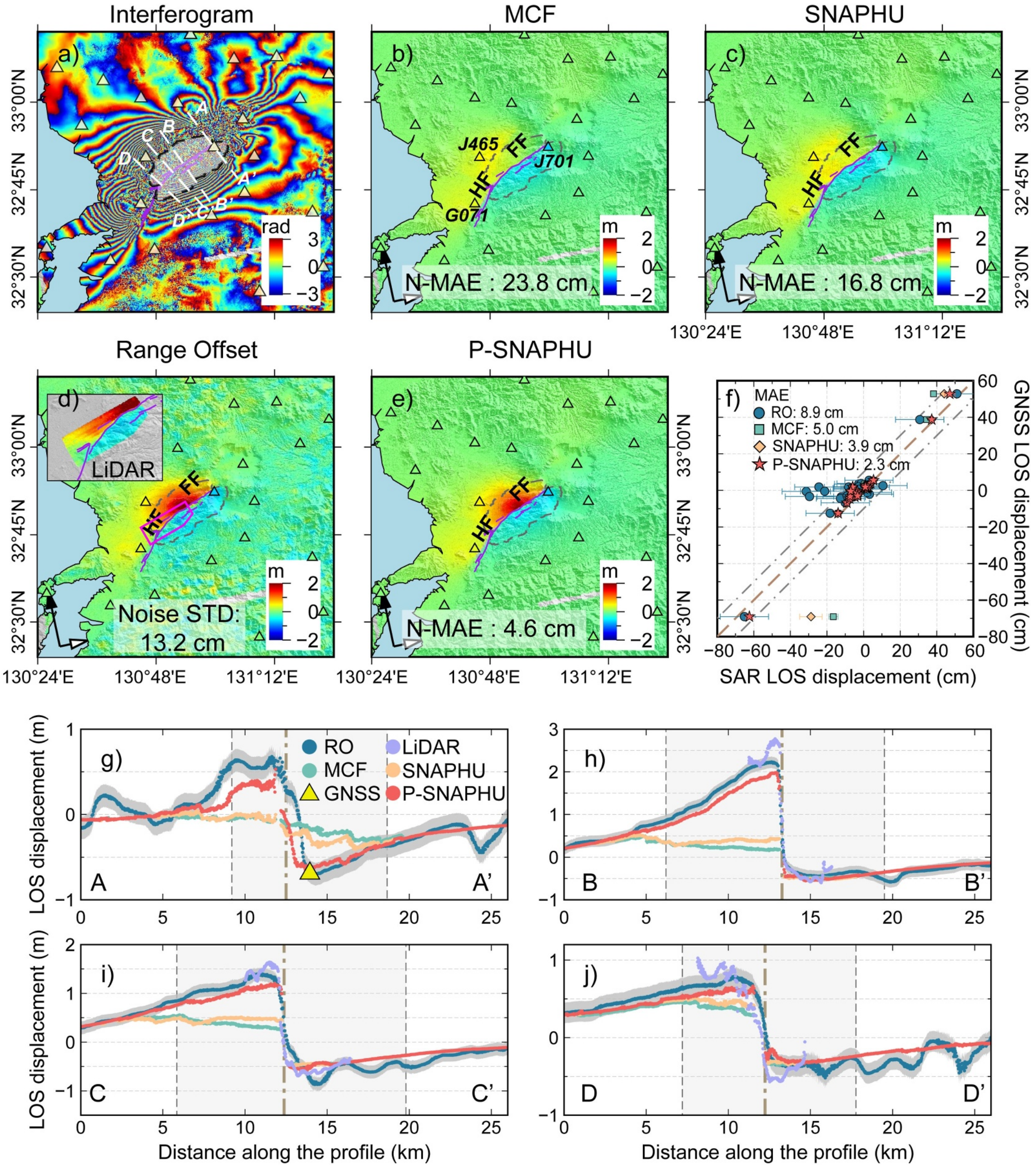

Figure 8. Unwrapped maps of the ascending interferogram from the 2016 Kumamoto earthquake. (a) The wrapped interferogram. Yellow triangles indicate available global navigation satellite system (GNSS) sites for recording the coseismic displacements. (b, c) The unwrapped coseismic deformation using MCF and SNAPHU, respectively. (d) The calculated coseismic range offset superposed on an elevation shadow map. The magenta line denotes LiDAR data coverage, shown in the upper left inset. (e) The unwrapped coseismic deformation using P-SNAPHU. The positive (red) and negative (blue) values indicate relative ground motion away from and toward the SAR satellite, respectively. The colored triangles in (b–e) display the GNSS displacements projected to the LOS direction. The purple lines in (a–e) outline the fault traces mapped by field investigation (Geological Survey of Japan, 2016: https://gbank.gsj.jp/activefault/search). The black dashed lines in (a–e) depict the separated near-field boundary by saliency extraction. (f) Comparison of projected GNSS LOS displacements from all 23 stations and the SAR LOS displacements. (g–j) Fault perpendicular profiles (AA'–DD') in (a) of LOS displacement derived from different data sources. The shading boxes denote the near-field areas, and the brown dash lines represent the locations of the surface ruptures. FF, the Futagawa Fault. HF, the Hinagu fault. RO, range offset. N-MAE is the mean absolute error between 3 near-field GNSS stations (with text labels in (b)) and the Interferometric Synthetic Aperture Radar (InSAR) unwrapped result. MAE is the mean absolute error between all 23 GNSS stations and the InSAR unwrapped result.

other methods. Profile BB' demonstrates the effectiveness of the proposed method in accurately restoring the deformation characteristics of a secondary fault, as found in Figures 9d and 9e. Profiles CC' and DD' manifest that the P-SNAPHU result within the LiDAR-constrained area closely mirrors the LiDAR data and remains impervious to the speckle noise of range offset.

Table 3
Comparison of Coseismic LOS Deformations Obtained by Different Methods and Near-Field GNSS Sites for the 2016 Kumamoto Earthquake

GNSS station	GNSS	Range offset	MCF	SNAPHU	P-SNAPHU
Ascending LOS deformation (cm)					
J071	38.7	30.7	34.4	37.2	37.2
J465	52.8	51.0	38.2	44.1	47.1
J701	−69.1	−65.1	−16.5	−28.8	−62.4
Descending LOS deformation (cm)					
J465	−24.6	−24.6	−23.8	−22.2	−22.2
J701	17.0	−3.6	−0.0	2.1	12.3
J703	16.7	13.8	17.0	15.6	16.8
J704	14.5	8.0	13.5	13.5	13.5

The 2.3 cm MAE in the ascending and descending Sentinel-1 interferograms obtained by P-SNAPHU is similar to the 2.0 cm accuracy obtained by Baek et al. (2018) using the offset-based minishing strategy on ALOS2 interferograms. This indicates a significant advancement in C-band phase unwrapping with our method, especially considering that the minishing strategy can not be applied to Sentinel-1 interferograms. It is worth mentioning that the ALOS2 unwrapped results showed a region of "linear surface rupture" (Baek et al., 2018), while this is not the focus of our findings, as we assume the phase continuity is maintained in the far field during the PGR step.

4.3. The 2019 Ridgecrest Earthquake Sequence

Within 34 hr between 4 and 6 July, 2019, a foreshock-mainshock earthquake sequence of *Mw* 6.4 and 7.1 occurred at Ridgecrest in the Eastern California Shear Zone, southern California. This event ruptured two conjugate faults in this region. The long rupture trends roughly northwest–southeast, while the short rupture is nearly perpendicular to the former, trending northeast–southwest. The two rupture faults were dominated by right-lateral and left-lateral strike slips (L. He et al., 2022; X. Xu et al., 2020). Field and remote-sensing surveys revealed the presence of many branch ruptures in the vicinity (Figure 10). The near-field decoherence of the interferograms for this sequence is not prominent (Figures 10a and 11a). These interferograms can be unwrapped using traditional methods with plausible results. The estimated STDs of noise for the ascending and descending range offsets are 7.3 and 11.0 cm, respectively, indicating that range offsets can provide reliable prior constraints in the P-SNAPHU method. Given the relatively small deformation scale and low speckle noise in these two cases (Figures 10d and 11d), we optimized the unwrapped results by adjusting the threshold values for the two key processing steps (Table 1).

The deformation characteristics of the P-SNAPHU unwrapped results from both the ascending and descending orbits were consistent with the multisegment surface rupture traces, showing noteworthy deformation differences on both sides of the ruptures (Figures 10e and 11e). The MAEs between all 7 GNSS stations and the P-SNAPHU unwrapped results are 2.2 and 1.3 cm for ascending and descending data, respectively, while the MAEs between GNSS and range offsets are 2.3 and 2.5 cm, respectively. Limited by the distribution of local GNSS stations, we could not quantitatively compare the differences between the three unwrapping methods in the near field. The unwrapping results obtained using different methods were identical for all seven GNSS sites (Figures 10f and 11f). However, the three selected profiles for each orbit show some divergence in the near field among the different sources (Figures 10g, 10h, 11g and 11h). In the AA' and BB' profiles of the ascending results, our method is closer to the range offset in the local deformation area near the surface ruptures, the solution of which is nearly 20 cm larger than that of traditional methods. The ascending BB' and CC' profiles also show that when coherence is high, our results remain resilient to the influence of erroneous prior information from the range offset, and the results can maintain consistency with those of traditional methods. The advantage of the P-SNAPHU method was more pronounced in the descending interferogram because the deformation scale was larger. Particularly in the CC' profile (Figure 11i), the P-SNAPHU method effectively captured the deformation characteristics of two surface ruptures in the local area, a task that is challenging for conventional methods.

In existing studies of this seismic event, L. He et al. (2022) utilized the traditional MCF method with a near-field mask to unwrap the same interferograms, while X. Xu et al. (2020) applied the SNAPHU method with masking and manually adjusted the optimal discontinuity value. In contrast, P-SNAPHU does not require manual intervention in selecting appropriate masking areas and the discontinuity parameter, resulting in a more comprehensive deformation field. Implementing the P-SNAPHU method also allows for the generation of higher-precision InSAR time series for the 2019 Ridgecrest earthquake sequence, facilitating a better estimation of deformation throughout each stage of the earthquake cycle (Guns et al., 2022).

5. Discussions

5.1. The Resistibility of P-SNAPHU to Raw Noise of Range Offsets

The earthquake cases show that the P-SNAPHU method can resist the noise of range offsets, particularly under the circumstances of good coherence or a far field. To deeply explore whether this resistance stems from the

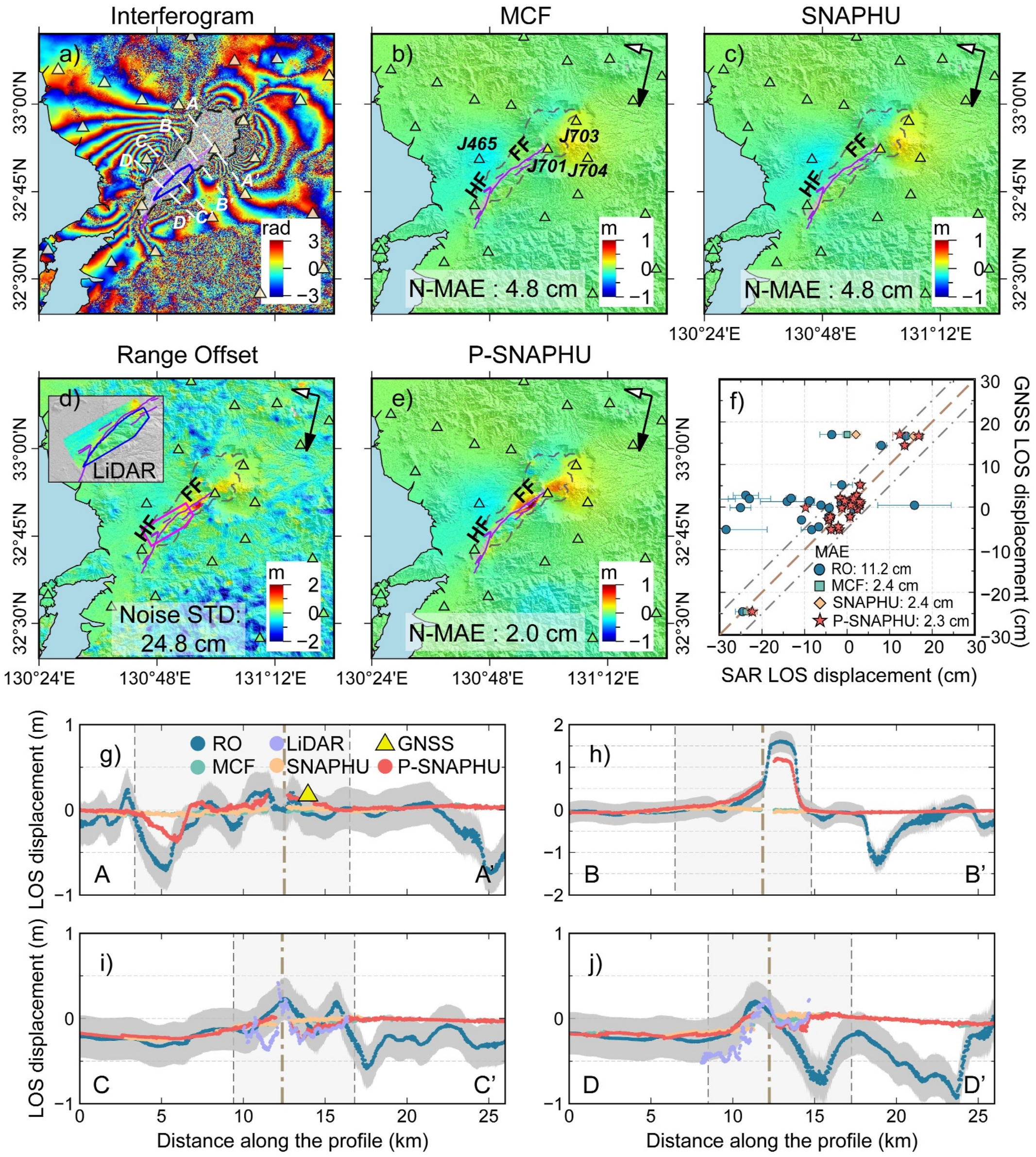

Figure 9. Similar to Figure 8 but for the descending interferogram from the 2016 Kumamoto earthquake. The blue lines in (a, d) depict the footprint of LiDAR prior information used for P-SNAPHU unwrapping.

unwrapping method itself or from the individual step before phase unwrapping and to understand the impact of prior constraints with various noise levels in different scenarios on the unwrapping accuracy, we provide the following experiments for clarification. We conducted simulation experiments for two cases, dense fringes, and sparse fringes, to simulate near-field and far-field scenarios, respectively. In each case, we applied four different levels of decoherence noise to the fringes, and the theoretical average coherence values were set to 0.4, 0.6, 0.8, and 1.0 (see Figure S7 in Supporting Information S1). Subsequently, we used simulated range offsets with noise STD ranging from 1 to 30 cm for unwrapping. To analyze the impact of noise separately, we did not conduct any preprocessing steps such as MFHP and PGR but used the original gradients directly. The coherence threshold was also not applied to highlight the effect of raw range offset noises on phase unwrapping. The RMSEs for the corresponding unwrapped results were calculated as indicators of unwrapping accuracy (Figures 12a and 12b).

First, we discuss the performance of unwrapping dense fringes. Lower coherence values corresponded to larger RMSEs and diminished resistance to noise in the range offsets. This correlation can be explained by the lower coherence levels signifying elevated noise, making the unwrapped results more vulnerable to disruptions from

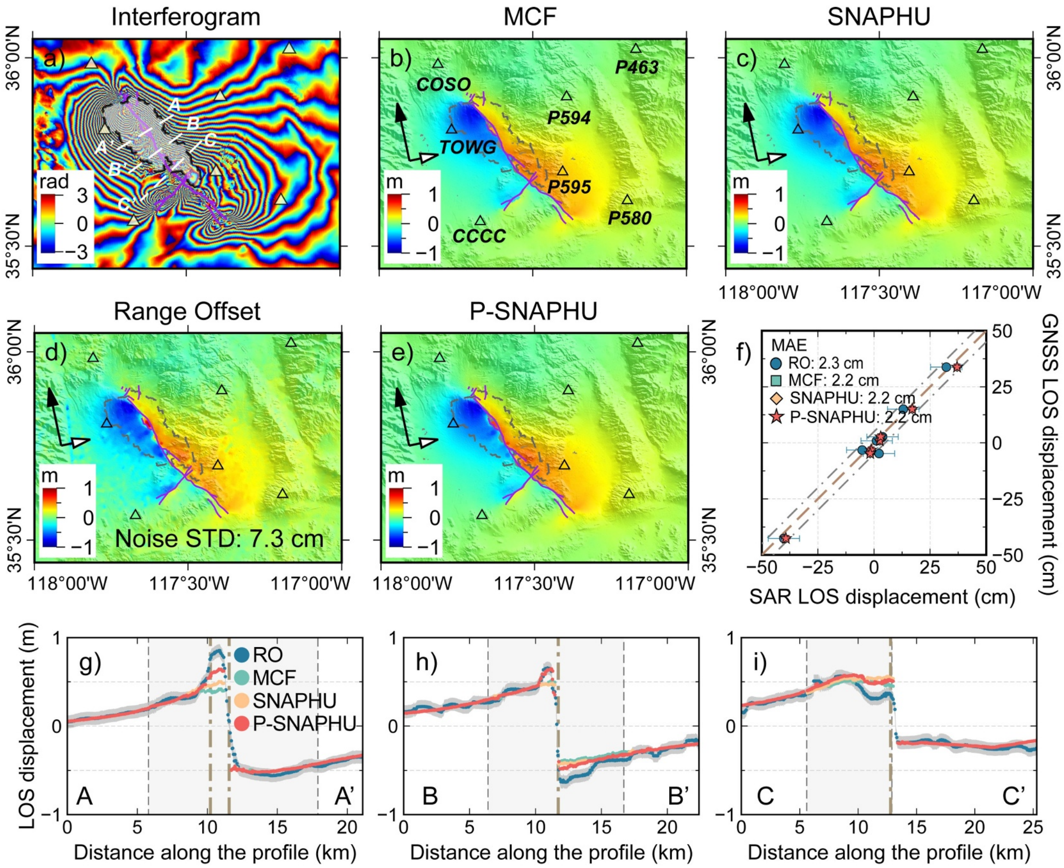

Figure 10. Unwrapped maps of the ascending interferogram from the 2019 Ridgecrest earthquake sequence. (a) The wrapped interferogram. Yellow triangles indicate available global navigation satellite system (GNSS) sites for recording the coseismic displacements. (b, c) The unwrapped coseismic deformation using MCF and SNAPHU, respectively. (d) The calculated coseismic range offset superposed on an elevation shadow map. (e) The unwrapped coseismic deformation using P-SNAPHU. The positive (red) and negative (blue) values indicate relative ground motion away from and toward the SAR satellite, respectively. The colored triangles in (b–e) display the GNSS displacements projected to the LOS direction. The purple lines in (a–e) outline the fault ruptures mapped by field investigation. The black dashed lines in (a–e) depict the separated near-field boundary by saliency extraction. (f) Comparison of projected GNSS LOS displacements from all 7 stations and the SAR LOS displacements. (g–i) Fault perpendicular profiles (AA'–CC') in (a) of LOS displacement derived from different data sources. The shading boxes denote the near-field areas, and the brown dash lines represent the locations of the surface ruptures. RO, range offset. MAE is the mean absolute error between all 7 GNSS stations and the Interferometric Synthetic Aperture Radar unwrapped result.

prior information with noise. Furthermore, prior information was not always useful for phase unwrapping. When the coherence is high (above 0.8), only prior information with a very small noise STD can positively affect unwrapping (the inset in Figure 12a). When the coherence is relatively low, prior information with a relatively small noise STD can effectively improve unwrapping accuracy. However, when the coherence is poor (below 0.6), the role of prior information becomes limited because the decoherence noise is too serious to be corrected. Second, we found that prior information with noise always plays a negative role for sparse fringes compared to SNAPHU because sparse fringes mean small deformation gradients and can be directly unwrapped under the phase continuity assumption. If the standard deviation of the noise in the prior data was higher than the amount of deformation, there was no clear correlation between coherence levels and the accuracy of unwrapping. Notably, in both cases, even with a mean coherence of 1.0, the noise STDs of the range offsets exceeding 8 cm resulted in RMSEs exceeding 5 cm, which is quite different from the simulated experimental results in Section 3 (Figure 4). This implies that the resistance shown in real cases is due to the key steps involved before unwrapping. Therefore, it is necessary to incorporate MFHP, PGR and use the coherence threshold within the workflow to improve the robustness of the P-SNAPHU method.

In addition, we measured the unwrapping time spent on the data set in these experiments (Figure 12c). We found a strong positive correlation between the unwrapping time of the P-SNAPHU and the increasing noise STD of the range offsets. In the case of the equivalent noise STD, sparser fringes and higher coherence tended to shorten the

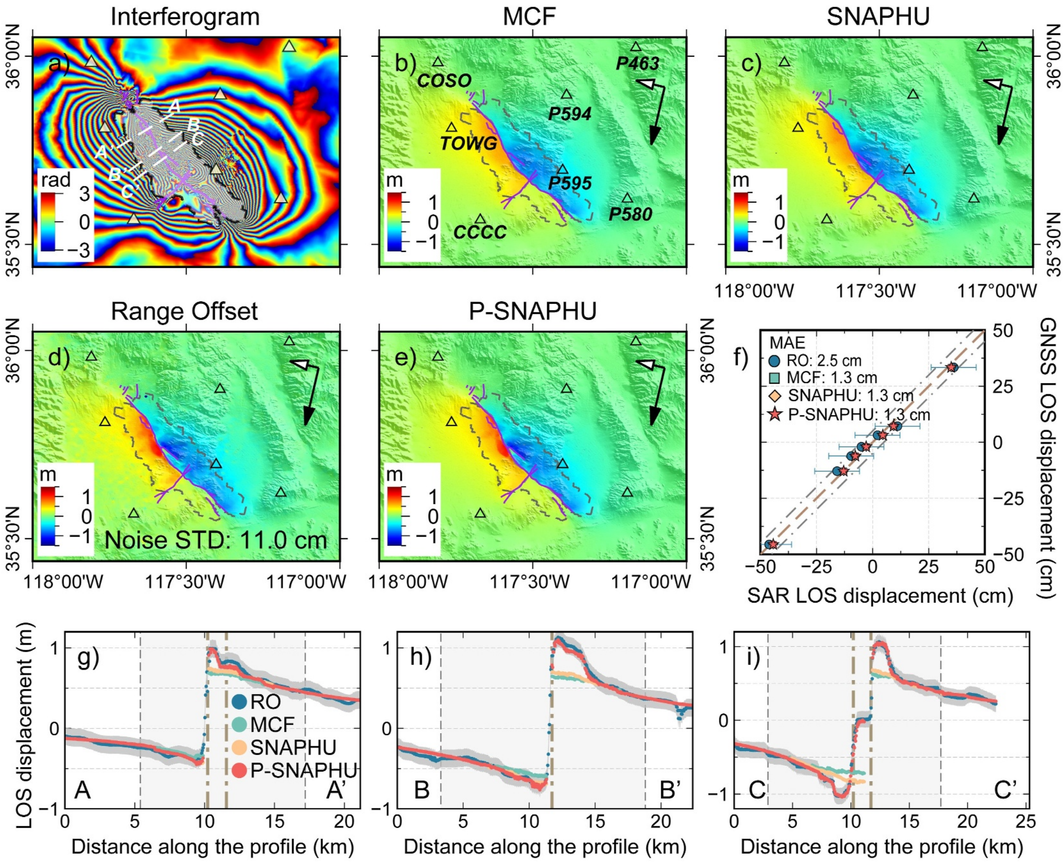

Figure 11. Similar to Figure 10 but for the descending interferogram from the 2019 Ridgecrest earthquake sequence.

unwrapping time. This phenomenon is easy to understand because the larger the errors in the wrapped phase or prior information, the more difficult it is for the objective function to determine the optimal solution, thereby incurring higher computational costs.

5.2. Different Impacts of T_{coh} and the Two Steps (MFHP and PGR) Before Unwrapping

Given that the coherence threshold T_{coh} directly determines whether to use prior gradients from range offsets to reconstruct the unwrapping cost functions and has an important impact on the unwrapping results. We discuss the

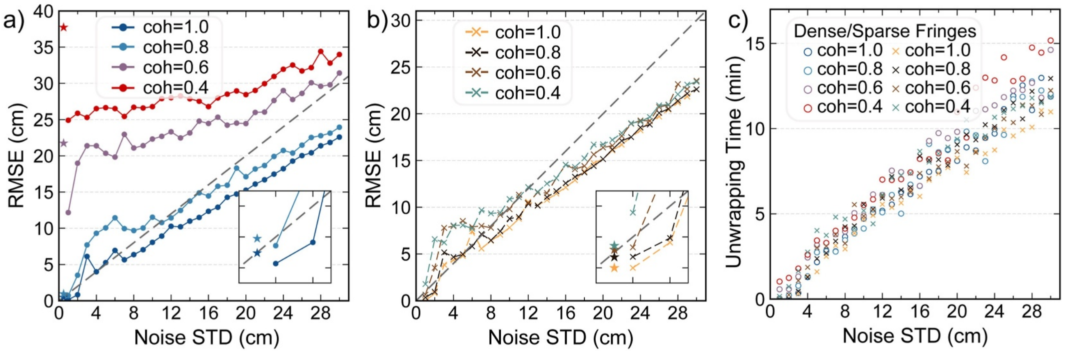

Figure 12. (a) RMSEs of unwrapped results for dense fringes with different coherence (0.4, 0.6, 0.8, and 1.0) under noise STDs of range offsets ranging from 0 to 30 cm. The stars represent the RMSEs SNAPHU obtained without prior range-offset gradients information. (b) Same with (a) but for sparse fringes. (c) The phase unwrapping time for fringes with different coherence under different noise STDs of range offsets.

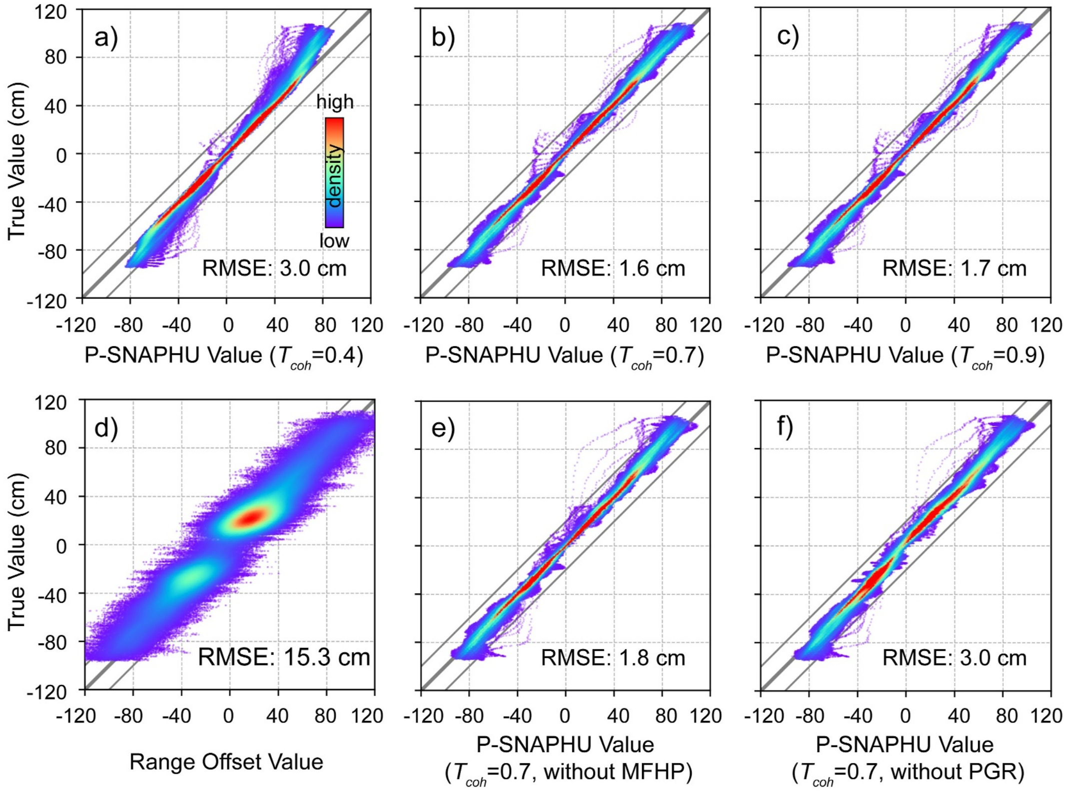

Figure 13. Scatter plots of unwrapped values by P-SNAPHU, range offset, and true values. (a–c) represent unwrapped values by P-SNAPHU with coherence threshold T_{coh} = 0.4, 0.7, and 0.9, respectively. (d) Represent range offset values. (e, f) represent unwrapped values by P-SNAPHU without MFHP and PGR, respectively.

most appropriate value for T_{coh}. Figures 13a–13c show the unwrapped scatter distribution and the corresponding RMSE for $T_{\mathrm{coh}} = 0.4$, 0.7, and 0.9, respectively. When T_{coh} is set to a low value, fewer gradients exist whose cost functions can be updated using prior information, resulting in poor unwrapped results. Conversely, if T_{coh} is excessively high, the prior constraints can become excessively strong, introducing unnecessary range offset noise and excess computing power. Therefore, we recommend T_{coh} takes 0.6–0.7 in the P-SNAPHU method. The comparison of results with varying T_{coh} for the 2023 Kahramanmaraş coseismic interferogram also proves this (Figure S10 in Supporting Information S1).

MFHP and PGR are the key steps before phase unwrapping in the P-SNAPHU workflow. To further discuss the impact of these two steps, we performed ablation experiments based on the simulated data shown in Figure 3. First, classic filtering is applied instead of the MFHP while keeping the other steps unchanged. A comparison between the obtained result and the true value is shown in Figure 13e, where points off the diagonal indicate a lower unwrapping accuracy. Errors occur mainly at both ends of the scatter point set with large absolute values. Second, simple average smoothing of the range offset gradients is used instead of PRG, as described in Section 2.3. A comparison of the results is presented in Figure 13f. Compared with Figure 13b, the differences are primarily concentrated at the waist of the scatter point set. Figure S11 in Supporting Information S1 provides a detailed comparison between the residual maps. Therefore, it can be inferred that the MFHP can enhance the accuracy of near-field solutions, whereas the PGR can greatly boost the overall accuracy.

5.3. Shallow Slip Deficit of the 2023 Kahramanmaraş Earthquake Doublet Using Different Masking Unwrapped Data

The SSD refers to the observation that the cumulative slip occurring in the shallow segments of faults, typically within a depth of 2 km, is significantly lower compared to the deeper sections. It is often ascribed to frictional characteristics such as velocity-strengthening behavior, off-fault deformation within narrow damage zones, and inelastic yielding influenced by lithological properties (Fialko et al., 2005). Accurate determination of the SSD is necessary for understanding the mechanisms underlying seismic activity and evaluating associated risk. However, some studies have shown that the SSD might be an artifact resulting from inversion bias caused by the absence of near-field deformation data (Ma et al., 2024; Marchandon et al., 2021; X. Xu et al., 2016).

The assessment of the SSD of the 2023 Kahramanmaraş earthquake doublet remains controversial in various studies, with estimates ranging from negligible to nearly 50% (Jia et al., 2023; Ma et al., 2024; Y. Zhang et al., 2023). Here, we conducted slip distribution inversion for this event using both ascending and descending data unwrapped by P-SNAPHU. To investigate the influence of different unwrapping methods on slip distribution, we masked regions with coherence values below 0.8 to represent results obtained from the conventional method (Figure S12 in Supporting Information S1). We set up the geometry of the faults system as fault F1–F7 based on previous studies (L. He et al., 2023; Y. Zhang et al., 2023), with dip angles of F1–F5 assumed to be 90°, and those of F6 and F7 set at 62° to the north and 60° to the west, respectively. The results of forward modeling for the two coseismic slip models align well with the available data (Figures S12 and S13 in Supporting Information S1). Minor discrepancies in the unmasked model's residuals are observed near fault intersections, potentially attributable to the simplifications made in the modeling process.

The results show that the slip model incorporating masking results in an underestimation of overall slip, with an average slip nearly 4% lower compared to the model without masking (Figure 14c). The discrepancy in shallow slip magnitude between the masked and unmasked models is most pronounced at specific locations, such as the western end of F6 and the middle of F3, where the difference reaches nearly 3 m (as indicated by black arrows in Figure 14). These regions coincide with the masked near-field data, suggesting that the absence of such data on a large scale can lead to a significant underestimation of the shallow slip magnitude. Moreover, we find that the absence of near-field data reduces the ability to finely characterize shallow slip (e.g., F1 and F2), while the unmasked model reveals more varied slip distributions within a depth of 10 km.

Furthermore, an analysis of the SSD between the two models reveals that the unmasked model has an SSD of approximately 7%, whereas the masked model shows negligible SSD (Figure 14c). To test the impact of spatial distribution of masked areas in the near field on the SSD estimation, we re-inverted the slip distribution using masks with varying coverage ranges, and consistently found SSDs close to zero. This indicates that the influence of missing near-field data on SSD estimation may be subject to various factors such as earthquake scenarios and model resolution (Ma et al., 2024), rather than a fixed overestimation (Marchandon et al., 2021; X. Xu et al., 2016). In addition, the observed 7% SSD aligns with the previous study by Ma et al. (2024), that the 2023 Kahramanmaraş earthquake doublet had a relatively minor SSD, and the absence of near-field InSAR deformation indeed impacted the accurate estimation of SSD.

5.4. Contributions and Prospects of the P-SNAPHU Method

Using three real earthquake cases with different degrees of decorrelation, we found that the P-SNAPHU method achieved positive and complete results in various scenarios. Complete C-band InSAR deformation maps with high unwrapping accuracy obtained by the P-SNAPHU play a crucial role in coseismic studies. L-band SAR data are scarce for medium-to-large earthquakes, and the complete C-band InSAR deformation field can provide a richer data source with multiple observational perspectives for three-dimensional deformation calculations (Liu et al., 2019). Furthermore, compared with range offsets with speckle noise, the deformation fields unwrapped by P-SNAPHU are smoother overall, which is beneficial for data downsampling and improves the stability of the coseismic slip distribution inversion (H. Gao et al., 2021). Using the P-SNAPHU method proposed in this study, C-band coseismic InSAR data can be more fully utilized and contribute significantly to understanding the mechanisms of seismic events.

In addition, we discuss the scalability of the proposed method. First, although P-SNAPHU was designed for unwrapping coseismic interferograms, it can be effective for handling other intractable C-band interferograms that are decoherent owing to large gradient deformations, such as volcanoes, landslides, glaciers, and mining. Second, the unwrapping case of the 2016 Kumamoto descending interferogram confirmed that LiDAR data can also be used as prior information in addition to range offsets. Thus, this method can be combined with other available and reliable external data, such as dense GNSS or prior mathematical models. Third, the case of the 2023 Kahramanmaraş earthquake proves that P-SNAPHU can effectively suppress the long-distance propagation of unwrapping errors. We consider that it also has the potential to be applied to wide-area interferograms, such as interseismic interferograms, where deformation gradients are small, but other factors, cause large-scale

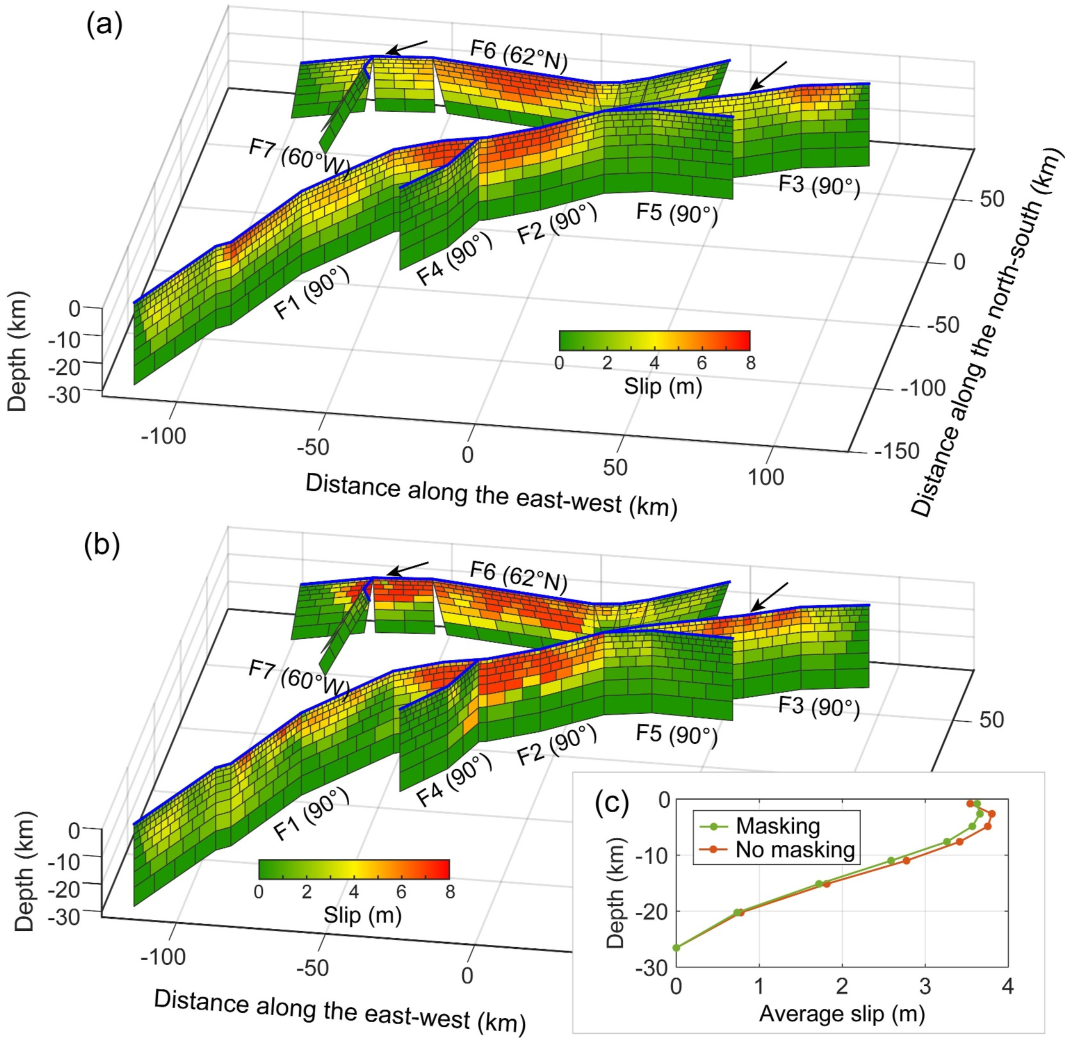

Figure 14. (a, b) Coseismic slip distribution for the 2023 Kahramanmaras earthquake doublet with masked and unmasked unwrapped data, respectively. (c) The comparison of average slip using full and masking observations.

decorrelations. Therefore, we believe that when diverse two-dimensional and three-dimensional unwrapping methods are well developed, such unwrapping ideas based on prior information of external data will be useful in addressing the remaining tricky problems.

This study also has certain limitations. The examination of the unwrapped results of the 2016 Kumamoto earthquake in Section 4.2 revealed that the inadequate separation of the near field in PGR and the uncontrolled decorrelated noise in interferograms are the main causes of the skewed findings. Besides, the assumption that the far field conforms to the phase continuity limits the identification of small linear ruptures. Therefore, potential enhancements could focus on intelligently segregating the near field, filtering coseismic interferograms in the near field, and accurately distinguishing noise in range offset priors.

6. Conclusions

We developed an improved phase unwrapping method, P-SNAPHU, for C-band coseismic interferograms using prior gradients of range offsets. The P-SNAPHU method involves three critical steps: (a) medial filtering of homogeneous pixels, (b) prior gradient refinement, and (c) prior-guided unwrapping. These steps can yield reliable prior gradients by processing noisy range offsets to constrain the shape of the PDFs with low coherence in phase unwrapping. Both the synthetic and real cases demonstrate that the P-SNAPHU method can effectively restore deformation in the non-unwrappable regions of the near field and suppress the propagation of unwrapping errors. Validating by the GNSS data, in the 2023 Kahramanmaraş, 2016 Kumamoto, and 2019 Ridgecrest earthquake events, the average unwrapping error can be reduced to 7.2, 2.3, and 1.8 cm, respectively. The 2023 Kahramanmaraş and 2016 Kumamoto events show an 84% and 34% increase in average accuracy, respectively, compared to the traditional algorithms. We further discussed the resistance of this method to range offsets noise and found the great impacts of the key steps on unwrapping accuracy. This method will further promote InSAR-based coseismic research and offer more reliable deformation maps for fault modeling. P-SNAPHU can be employed in other applications with steep gradients (e.g., volcanoes and landslides). More work is needed in improving the separation of near-field signals and reducing noise in range-offset.

Data Availability Statement

Supporting Information includes Figures S1–S13 and Table S1 in Supporting Information S1. The open source software SNAPHU is obtained from C. W. Chen and Zebker (2024). Codes for geophysical inversion are from Jin (2021). The codes of the proposed P-SNAPHU method in this paper are available at K. Jiang and Xu (2024).

Acknowledgments

We greatly thank the Editor, the Associate Editor and the two anonymous reviewers for their thorough and constructive comments that greatly helped improve this work. This research was supported by the National Natural Science Foundation of China (No. 42174023), the National Science Fund for Distinguished Young Scholars (41925016), the Natural Science Foundation of Hunan Province (2024JJ3031). We thank the European Space Agency for open access to Sentinel-1 data. We deeply thank Yingfeng Zhang, Yukitoshi Fukahata and the Nevada Geodetic Laboratory for providing GNSS data. We acknowledge Ping He for providing LiDAR data. Figures in the paper were generated by the Generic Mapping Tools (Wessel et al., 2019), python and matplotlib.

References

Baek, W.-K., & Jung, H.-S. (2020). Precise three-dimensional deformation retrieval in large and complex deformation areas via integration of offset-based unwrapping and improved multiple-aperture SAR interferometry: Application to the 2016 Kumamoto earthquake. *Engineering*, *6*(8), 927–935. https://doi.org/10.1016/j.eng.2020.06.012

Baek, W.-K., Jung, H.-S., & Chae, S.-H. (2018). Feasibility of ALOS2 PALSAR2 offset-based phase unwrapping of SAR interferogram in large and complex surface deformations. *IEEE Access*, *6*, 45951–45960. https://doi.org/10.1109/ACCESS.2018.2865799

Bamler, R., & Eineder, M. (2005). Accuracy of differential shift estimation by correlation and split-bandwidth interferometry for wideband and delta-k SAR systems. *IEEE Geoscience and Remote Sensing Letters*, *2*(2), 151–155. https://doi.org/10.1109/LGRS.2004.843203

Barbot, S., Luo, H., Wang, T., Hamiel, Y., Piatibratova, O., Muhammad, T., et al. (2023). Slip distribution of the February 6, 2023 Mw 7.8 and Mw 7.6, Kahramanmaraş, Turkey earthquake sequence in the east Anatolian fault zone. *Seismica*, *2*(3). https://doi.org/10.26443/seismica.v2i3.502

Barnhart, W. D., Murray, J. R., Briggs, R. W., Gomez, F., Miles, C. P. J., Svarc, J., et al. (2016). Coseismic slip and early afterslip of the 2015 Illapel, Chile, earthquake: Implications for frictional heterogeneity and coastal uplift. *Journal of Geophysical Research: Solid Earth*, *121*(8), 6172–6191. https://doi.org/10.1002/2016jb013124

Bletery, Q., Cavalié, O., Nocquet, J. M., & Ragon, T. (2020). Distribution of interseismic coupling along the North and East Anatolian faults inferred from InSAR and GPS data. *Geophysical Research Letters*, *47*(16), e2020GL087775. https://doi.org/10.1029/2020GL087775

Bürgmann, R., Rosen, P. A., & Fielding, E. J. (2000). Synthetic aperture radar interferometry to measure Earth's surface topography and its deformation. *Annual Review of Earth and Planetary Sciences*, *28*(1), 169–209. https://doi.org/10.1146/annurev.earth.28.1.169

Bürgmann, R., Schmidt, D., Nadeau, R., d'Alessio, M., Fielding, E., Manaker, D., et al. (2000). Earthquake potential along the Northern Hayward fault, California. *Science*, *289*(5482), 1178–1182. https://doi.org/10.1126/science.289.5482.1178

Chen, C. W., & Zebker, H. A. (2000). Network approaches to two-dimensional phase unwrapping: Intractability and two new algorithms. *Journal of the Optical Society of America. A*, *17*(3), 401–414. https://doi.org/10.1364/JOSAA.17.000401

Chen, C. W., & Zebker, H. A. (2001). Two-dimensional phase unwrapping with use of statistical models for cost functions in nonlinear optimization. *Journal of the Optical Society of America. A*, *18*(2), 338–351. https://doi.org/10.1364/josaa.18.000338

Chen, C. W., & Zebker, H. A. (2002). Phase unwrapping for large SAR interferograms: Statistical segmentation and generalized network models. *IEEE Transactions on Geoscience and Remote Sensing*, *40*(8), 1709–1719. https://doi.org/10.1109/tgrs.2002.802453

Chen, C. W., & Zebker, H. A. (2024). SNAPHU: Statistical-cost, network-flow algorithm for phase unwrapping (version 2.0.7) [Software]. Retrieved from https://web.stanford.edu/group/radar/softwareandlinks/sw/snaphu/

Costantini, M. (1998). A novel phase unwrapping method based on network programming. *IEEE Transactions on Geoscience and Remote Sensing*, *36*(3), 813–821. https://doi.org/10.1109/36.673674

Dai, Y., Ng, A. H.-M., Wang, H., Li, L., Ge, L., & Tao, T. (2020). Modeling-assisted InSAR phase-unwrapping method for mapping mine subsidence. *IEEE Geoscience and Remote Sensing Letters*, *18*(6), 1059–1063. https://doi.org/10.1109/LGRS.2020.2991687

Elliott, J. R., Walters, R. J., & Wright, T. J. (2016). The role of space-based observation in understanding and responding to active tectonics and earthquakes. *Nature Communications*, *7*(1), 13844. https://doi.org/10.1038/ncomms13844

Feng, X., Chen, Z., Li, G., Ju, Q., Yang, Z., & Cheng, X. (2023). Improving the capability of D-InSAR combined with offset-tracking for monitoring glacier velocity. *Remote Sensing of Environment*, *285*, 113394. https://doi.org/10.1016/j.rse.2022.113394

Fialko, Y., Sandwell, D., Simons, M., & Rosen, P. (2005). Three-dimensional deformation caused by the Bam, Iran, earthquake and the origin of shallow slip deficit. *Nature*, *435*(7040), 295–299. https://doi.org/10.1038/nature03425

Fielding, E. J., Liu, Z., Stephenson, O. L., Zhong, M. Y., Liang, C. R., Moore, A., et al. (2020). Surface deformation related to the 2019 Mw 7.1 and 6.4 Ridgecrest earthquakes in California from GPS, SAR interferometry, and SAR pixel offsets. *Seismological Research Letters*, *91*(4), 2035–2046. https://doi.org/10.1785/0220190302

Fujiwara, S., Morishita, Y., Nakano, T., Kobayashi, T., & Yarai, H. (2017). Non-tectonic liquefaction-induced large surface displacements in the Aso Valley, Japan, caused by the 2016 Kumamoto earthquake, revealed by ALOS-2 SAR. *Earth and Planetary Science Letters*, *474*, 457–465. https://doi.org/10.1016/j.epsl.2017.07.001

Fukahata, Y., & Hashimoto, M. (2016). Simultaneous estimation of the dip angles and slip distribution on the faults of the 2016 Kumamoto earthquake through a weak nonlinear inversion of InSAR data. *Earth Planets and Space*, *68*(1), 1–10. https://doi.org/10.1186/s40623-016-0580-4

Gao, H., Liao, M., & Feng, G. (2021). An improved Quadtree sampling method for InSAR seismic deformation inversion. *Remote Sensing*, *13*(9), 1678. https://doi.org/10.3390/rs13091678

Gao, Y., Zheng, N., Li, S., Zhang, Y., Zhang, Q., & Zhang, S. (2023). A novel two-step DInSAR phase-unwrapping for large gradient mining deformation. In *IEEE journal on miniaturization for air and Space systems*. https://doi.org/10.1109/JMASS.2023.3305242

Geological Survey of Japan. (2016). Active fault database of Japan. [Dataset]. https://gbank.gsj.jp/activefault/search

Ghiglia, D. C., & Pritt, M. D. (1998). *Two-dimensional phase unwrapping: Theory, algorithms, and software*. John Wiley and Sons.

Guns, K., Xu, X., Bock, Y., & Sandwell, D. (2022). GNSS-corrected InSAR displacement time-series spanning the 2019 Ridgecrest, CA earthquakes. *Geophysical Journal International*, *230*(2), 1358–1373. https://doi.org/10.1093/gji/ggac121

He, L., Feng, G., Hu, J., Xu, W., Liu, J., Li, Z., et al. (2022). Surface displacement and source model separation of the two strongest earthquakes during the 2019 Ridgecrest sequence: Insights from InSAR, GPS, and optical data. *Journal of Geophysical Research: Solid Earth*, *127*(2), e2021JB022779. https://doi.org/10.1029/2021JB022779

He, L., Feng, G., Xu, W., Wang, Y., Xiong, Z., Gao, H., & Liu, X. (2023). Coseismic kinematics of the 2023 Kahramanmaras, Turkey earthquake sequence from InSAR and optical data. *Geophysical Research Letters*, *50*(17), e2023GL104693. https://doi.org/10.1029/2023GL107788

He, P., Wen, Y., Xu, C., & Chen, Y. (2019). Complete three-dimensional near-field surface displacements from imaging geodesy techniques applied to the 2016 Kumamoto earthquake. *Remote Sensing of Environment*, *232*, 111321. https://doi.org/10.1016/j.rse.2019.111321

Hu, J., Liu, J., Li, Z., Zhu, J., Wu, L., Sun, Q., & Wu, W. (2021). Estimating three-dimensional coseismic deformations with the SM-VCE method based on heterogeneous SAR observations: Selection of homogeneous points and analysis of observation combinations. *Remote Sensing of Environment*, *255*, 112298. https://doi.org/10.1016/j.rse.2021.112298

Hussain, E., Wright, T. J., Walters, R. J., Bekaert, D. P., Lloyd, R., & Hooper, A. (2018). Constant strain accumulation rate between major earthquakes on the North Anatolian Fault. *Nature Communications*, *9*(1), 1392. https://doi.org/10.1038/s41467-018-03739-2

Itoh, K. (1982). Analysis of the phase unwrapping algorithm. *Applied Optics*, *21*(14), 2470. https://doi.org/10.1364/AO.21.002470

Itti, L., Koch, C., & Niebur, E. (1998). A model of saliency-based visual attention for rapid scene analysis. *IEEE Transactions on Pattern Analysis and Machine Intelligence*, *20*(11), 1254–1259. https://doi.org/10.1109/34.730558

Jia, Z., Jin, Z., Marchandon, M., Ulrich, T., Gabriel, A.-A., Fan, W., et al. (2023). The complex dynamics of the 2023 Kahramanmaraş, Turkey, Mw 7.8-7.7 earthquake doublet. *Science*, *381*(6661), 985–990. https://doi.org/10.1126/science.adi0685

Jiang, H. J., Feng, G. C., Wang, T., & Bürgmann, R. (2017). Toward full exploitation of coherent and incoherent information in Sentinel-1 TOPS data for retrieving surface displacement: Application to the 2016 Kumamoto (Japan) earthquake. *Geophysical Research Letters*, *44*(4), 1758–1767. https://doi.org/10.1002/2016gl072253

Jiang, K., & Xu, W. B. (2024). P-SNAPHU (version 1) [Software]. *Zenodo*. https://doi.org/10.5281/zenodo.12818649

Jin, Z. Y. (2021). Matlab routines for inversion of space geodetic data for subsurface fault slip (Version 1) [Software]. *Zenodo*. https://doi.org/10.5281/zenodo.5528322

Li, S., Wang, X., Tao, T., Zhu, Y., Qu, X., Li, Z., et al. (2023). Source model of the 2023 Turkey earthquake sequence imaged by sentinel-1 and GPS measurements: Implications for heterogeneous fault behavior along the East Anatolian Fault zone. *Remote Sensing*, *15*(10), 2618. https://doi.org/10.3390/rs15102618

Liu, C., Lay, T., Wang, R., Taymaz, T., Xie, Z., Xiong, X., et al. (2023a). Complex multi-fault rupture and triggering during the 2023 earthquake doublet in southeastern Türkiye. *Nature Communications*, *14*(1), 5564. https://doi.org/10.1038/s41467-023-41404-5

Liu, H., Xie, L., Zhao, G., Ali, E., & Xu, W. (2023b). A joint InSAR-GNSS workflow for correction and selection of interferograms to estimate high-resolution interseismic deformations. *Satellite Navigation*, *4*(1), 14. https://doi.org/10.1186/s43020-023-00105-6

Liu, J. H., Hu, J., Li, Z. W., Ma, Z. F., Wu, L. X., Jiang, W. P., et al. (2022). Complete three-dimensional coseismic displacements due to the 2021 Maduo earthquake in Qinghai Province, China from Sentinel-1 and ALOS-2 SAR images. *Science China Earth Sciences*, *65*(4), 687–697. https://doi.org/10.1007/s11430-021-9868-9

Liu, J. H., Hu, J., Xu, W. B., Li, Z. W., Zhu, J. J., Ding, X. L., & Zhang, L. (2019). Complete three-dimensional coseismic deformation field of the 2016 central Tottori earthquake by Integrating left-and right-looking InSAR observations with the improved SM-VCE method. *Journal of Geophysical Research: Solid Earth*, *124*(11), 12099–12115. https://doi.org/10.1029/2018jb017159

Liu, Y., Zhang, Y., Wen, Y. M., & Yang, J. Y. (2023c). Coseismic and postseismic fault slip characteristics of the 2020 Mw 6.3 Nima earthquake. *Reviews of Geophysics and Planetary Physics (in Chinese)*, *54*(6), 643–652. https://doi.org/10.19975/j.dqyxx.2022-078

Lyu, M., Chen, K., Xue, C., Zang, N., Zhang, W., & Wei, G. (2022). Overall subshear but locally supershear rupture of the 2021 Mw 7.4 Maduo earthquake from high-rate GNSS waveforms and three-dimensional InSAR deformation. *Tectonophysics*, *839*, 229542. https://doi.org/10.1016/j.tecto.2022.229542

Ma, Z., Li, C., Jiang, Y., Chen, Y., Yin, X., Aoki, Y., et al. (2024). Space geodetic insights to the dramatic stress rotation induced by the February 2023 Turkey-Syria earthquake doublet. *Geophysical Research Letters*, *51*(6), e2023GL107788. https://doi.org/10.1029/2023GL107788

Marchandon, M., Hollingsworth, J., & Radiguet, M. (2021). Origin of the shallow slip deficit on a strike slip fault: Influence of elastic structure, topography, data coverage, and noise. *Earth and Planetary Science Letters*, *554*, 116696. https://doi.org/10.1016/j.epsl.2020.116696

Massonnet, D., Rossi, M., Carmona, C., Adragna, F., Peltzer, G., Feigl, K., & Rabaute, T. (1993). The displacement field of the Landers earthquake mapped by radar interferometry. *Nature*, *364*(6433), 138–142. https://doi.org/10.1038/364138a0

Metzger, S., Schurr, B., Ratschbacher, L., Sudhaus, H., Kufner, S. K., Schöne, T., et al. (2017). The 2015 Mw7. 2 Sarez strike-slip earthquake in the Pamir interior: Response to the underthrusting of India's western promontory. *Tectonics*, *36*(11), 2407–2421. https://doi.org/10.1002/2017tc004581

Milliner, C. W. D., Dolan, J. F., Hollingsworth, J., Leprince, S., Ayoub, F., & Sammis, C. G. (2015). Quantifying near-field and off-fault deformation patterns of the 1992 M-w 7.3 Landers earthquake. *Geochemistry, Geophysics, Geosystems*, *16*(5), 1577–1598. https://doi.org/10.1002/2014gc005693

Moore, J. D., Yu, H., Tang, C.-H., Wang, T., Barbot, S., Peng, D., et al. (2017). Imaging the distribution of transient viscosity after the 2016 Mw 7.1 Kumamoto earthquake. *Science*, *356*(6334), 163–167. https://doi.org/10.1126/science.aal3422

Nissen, E., Maruyama, T., Arrowsmith, J. R., Elliott, J. R., Krishnan, A. K., Oskin, M. E., & Saripalli, S. (2014). Coseismic fault zone deformation revealed with differential Lidar: Examples from Japanese M-w similar to 7 intraplate earthquakes. *Earth and Planetary Science Letters*, *405*, 244–256. https://doi.org/10.1016/j.epsl.2014.08.031

Perlin, K. (1985). An image synthesizer. *ACM Siggraph Computer Graphics*, *19*(3), 287–296. https://doi.org/10.1145/325165.325247

Scott, C. P., Arrowsmith, J. R., Nissen, E., Lajoie, L., Maruyama, T., & Chiba, T. (2018). The M7 2016 Kumamoto, Japan, earthquake: 3-D deformation along the fault and within the damage zone constrained from differential Lidar topography. *Journal of Geophysical Research: Solid Earth*, *123*(7), 6138–6155. https://doi.org/10.1029/2018jb015581

Shirahama, Y., Yoshimi, M., Awata, Y., Maruyama, T., Azuma, T., Miyashita, Y., et al. (2016). Characteristics of the surface ruptures associated with the 2016 Kumamoto earthquake sequence, central Kyushu, Japan. *Earth Planets and Space*, *68*(1), 1–12. https://doi.org/10.1186/s40623-016-0559-1

Sudhaus, H., & Sigurjón, J. (2009). Improved source modelling through combined use of InSAR and GPS under consideration of correlated data errors: Application to the June 2000 Kleifarvatn earthquake, Iceland. *Geophysical Journal International*, *176*(2), 389–404. https://doi.org/10.1111/j.1365-246X.2008.03989.x

Vajedian, S., Aflaki, M., Mousavi, Z., Ghods, A., Walker, R., & Maurer, J. (2023). Seismotectonic modeling of the 2017 Hojedk (Kerman) earthquake sequence from joint inversion of InSAR and offset tracking techniques. *Remote Sensing of Environment*, *288*, 113461. https://doi.org/10.1016/j.rse.2023.113461

Wang, T., Wei, S., Shi, X., Qiu, Q., Li, L., Peng, D., et al. (2018). The 2016 Kaikōura earthquake: Simultaneous rupture of the subduction interface and overlying faults. *Earth and Planetary Science Letters*, *482*, 44–51. https://doi.org/10.1016/j.epsl.2017.10.056

Wang, W., Liu, Y., Fan, X., Ma, C., & Shan, X. (2023). Coseismic deformation, fault slip distribution, and coulomb stress perturbation of the 2023 Türkiye-Syria earthquake doublet based on SAR offset tracking. *Remote Sensing*, *15*(23), 5443. https://doi.org/10.3390/rs15235443

Weiss, J. R., Walters, R. J., Morishita, Y., Wright, T. J., Lazecky, M., Wang, H., et al. (2020). High-resolution surface velocities and strain for Anatolia from Sentinel-1 InSAR and GNSS data. *Geophysical Research Letters*, *47*(17), e2020GL087376. https://doi.org/10.1029/2020GL087376

Wessel, P., Luis, J., Uieda, L., Scharroo, R., Wobbe, F., Smith, W. H., & Tian, D. (2019). The generic mapping tools version 6. *Geochemistry, Geophysics, Geosystems*, *20*(11), 5556–5564. https://doi.org/10.1029/2019GC008515

Wright, T. J., Lu, Z., & Wicks, C. (2003). Source model for the Mw 6.7, 23 October 2002, Nenana mountain earthquake (Alaska) from InSAR. *Geophysical Research Letters*, *30*(18), 1974. https://doi.org/10.1029/2003gl018014

Xu, W. B. (2017). Finite-fault slip model of the 2016 Mw 7.5 Chiloé earthquake, southern Chile, estimated from Sentinel-1 data. *Geophysical Research Letters*, *44*(10), 4774–4780. https://doi.org/10.1002/2017GL073560

Xu, W. B., Feng, G. C., Meng, L. S., Zhang, A. L., Ampuero, J. P., Bürgmann, R., & Fang, L. H. (2018). Transpressional rupture cascade of the 2016 Mw 7.8 Kaikoura earthquake, New Zealand. *Journal of Geophysical Research: Solid Earth*, *123*(3), 2396–2409. https://doi.org/10.1002/2017jb015168

Xu, X., Sandwell, D. T., & Smith-Konter, B. (2020). Coseismic displacements and surface fractures from Sentinel-1 InSAR: 2019 Ridgecrest earthquakes. *Seismological Research Letters*, *91*(4), 1979–1985. https://doi.org/10.1785/0220190275

Xu, X., Tong, X., Sandwell, D. T., Milliner, C. W. D., Dolan, J. F., Hollingsworth, J., et al. (2016). Refining the shallow slip deficit. *Geophysical Journal International*, *204*(3), 1867–1886. https://doi.org/10.1093/gji/ggv563

Yu, H. W., Lan, Y., Yuan, Z. H., Xu, J. Y., & Lee, H. (2019). Phase unwrapping in InSAR: A review. *IEEE Geoscience and Remote Sensing Magazine*, *7*(1), 40–58. https://doi.org/10.1109/mgrs.2018.2873644

Yue, H., Ross, Z. E., Liang, C. R., Michel, S., Fattahi, H., Fielding, E., et al. (2017). The 2016 Kumamoto Mw= 7.0 earthquake: A significant event in a fault–volcano system. *Journal of Geophysical Research: Solid Earth*, *122*(11), 9166–9183. https://doi.org/10.1002/2017jb014525

Zebker, H. A., & Villasenor, J. (1992). Decorrelation in interferometric radar echoes. *IEEE Transactions on Geoscience and Remote Sensing*, *30*(5), 950–959. https://doi.org/10.1109/36.175330

Zhang, Y., Shan, X., Zhang, G., Gong, W., Liu, X., Yin, H., et al. (2018). Source model of the 2016 Kumamoto, Japan, earthquake constrained by InSAR, GPS, and strong-motion data: Fault slip under extensional stress. *Bulletin of the Seismological Society of America*, *108*(5A), 2675–2686. https://doi.org/10.1785/0120180023

Zhang, Y., Tang, X., Liu, D., Taymaz, T., Eken, T., Guo, R., et al. (2023). Geometric controls on cascading rupture of the 2023 Kahramanmaraş earthquake doublet. *Nature Geoscience*, *16*(11), 1054–1060. https://doi.org/10.1038/s41561-023-01283-3

Zhao, Q., Jiang, F., Zhu, L., & Xu, J. (2023). Synthetic aperture radar interferometry–based Coseismic deformation and slip distribution of the 2022 Menyuan MS6. 9 earthquake in Qinghai, China. *Geodesy and Geodynamics*, *14*(6), 541–550. https://doi.org/10.1016/j.geog.2023.07.004